Current Opinion in Solid State and Materials Science xxx (xxxx) xxx

Contents lists available at ScienceDirect

Current Opinion in Solid State & Materials Science

journal homepage: www.elsevier.com/locate/cossms

Hydriding of titanium: Recent trends and perspectives in advanced characterization and multiscale modeling

Yakun Zhu [a,*], Tae Wook Heo [a], Jennifer N. Rodriguez [a], Peter K. Weber [a], Rongpei Shi [a], Bruce J. Baer [a], Felipe F. Morgado [b], Stoichko Antonov [c], Kyoung E. Kweon [a], Erik B. Watkins [d], Daniel J. Savage [d], James E. Chapman [a], Nathan D. Keilbart [a], Younggil Song [a], Qi Zhen [a], Baptiste Gault [b,e], Sven C. Vogel [d], Shohini T. Sen-Britain [a], Matthew G. Shalloo [a], Chris Orme [a], Michael Bagge-Hansen [a], Christopher Hahn [a], Tuan A. Pham [a], Digby D. Macdonald [f], S. Roger Qiu [a], Brandon C. Wood [a,*]

[a] Materials Science Division, Lawrence Livermore National Laboratory, Livermore, CA 94550, USA
[b] Department of Microstructure Physics and Alloy Design, Max-Planck Institut für Eisenforschung GmbH, Max-Planck-Str. 1, 40237 Düsseldorf, Germany
[c] National Energy Technology Laboratory, 1450 Queen Ave. SW, Albany, OR 97321, USA
[d] Los Alamos Neutron Science Center, Los Alamos National Laboratory, Los Alamos, NM 87545, USA
[e] Department of Materials, Royal School of Mines, Imperial College London, Prince Consort Road, London SW7 2BP, UK
[f] Department of Nuclear Engineering, University of California at Berkeley, Berkeley, CA 94720, USA

A B S T R A C T

Titanium (Ti) and its alloys are attractive for a wide variety of structural and functional applications owing to excellent specific strength, toughness and stiffness, and corrosion resistance. However, if exposed to hydrogen sources, these alloys are susceptible to hydride formation in the form of TiH_x ($0 < x \leq 2$), leading to crack initiation and mechanical failure due to lattice deformation and stress accumulation. The kinetics of the hydriding process depends on several factors, including the critical saturation threshold for hydrogen within Ti, the specific interaction of hydrogen with protective surface oxide, the rates of mass transport, and the kinetics of nucleation and phase transformation. Unfortunately, key knowledge gaps and challenges remain regarding the details of these coupled processes, which take place across vast ranges of time and length scales and are often difficult to probe directly. This work reviews recent advances in multiscale characterization and modeling efforts in Ti hydriding. We identify unanswered questions and key challenges, propose new perspectives on how to solve these remaining issues, and close knowledge gaps by discussing and demonstrating specific opportunities for integrating advanced characterization and multiscale modeling to elucidate chemistry and composition, microstructure phenomena, and macroscale performance and testing.

1. General overview of hydriding of Ti

1.1. Introduction to Ti

Titanium (Ti) and Ti-based alloys possess superior combined physical and mechanical properties in addition to good corrosion resistance, which make them outstanding materials for a variety of structural and functional applications [1–8]. For instance, the high specific strength (strength-to-weight ratio) and corrosion resistance make Ti a widely used material in aerospace (such as airframe parts and jet engine blades), automotive, and energy applications (such as petrochemical and nuclear-power-generation components) [3,5,6]. Because of their excellent biocompatibility *in vivo*, Ti alloys have also become increasingly attractive for biomedical applications [2,9].

Ti exists in two allotropic crystalline forms: the high-temperature β phase with a body-centered cubic (bcc) structure and the low-temperature α phase with a hexagonal close-packed (hcp) structure [5,8,10]. Consequently, Ti alloys can be categorized using a nomenclature based on the predominant phases within their microstructure at room temperature. Alloys consisting of mainly of the α phase are referred to as α-alloys (or near-α alloys if a small amount of β phase is present). Conversely, β-dominated Ti alloys are called β-alloys, whereas those featuring a mixture of α and β phases are called α/β alloys.

Alloying elements in Ti alloys usually act as α or β stabilizers, which are required to achieve the desired mechanical properties, including tensile strength, creep, and fracture toughness, as well as resistance to degradation modes such as fatigue crack propagation, stress-corrosion cracking, and oxidation [1,3,11,12]. Further optimization of

* Corresponding authors.
E-mail addresses: zhu15@llnl.gov (Y. Zhu), wood37@llnl.gov (B.C. Wood).

https://doi.org/10.1016/j.cossms.2022.101020
Received 29 January 2022; Received in revised form 21 June 2022; Accepted 1 July 2022
Available online 9 July 2022

mechanical properties can be achieved through thermal and mechanical treatments to engineer microstructures with desired sizes, shapes, spatial distributions, and interface coherency states of α precipitates within the β matrix. Although the microstructure is primarily composed of two simple phases, many different phase transformation pathways from β to α exist, providing ample opportunities for engineering and optimizing the microstructure towards specific applications. A commonly employed Ti metal is the unalloyed commercially pure (CP) Ti family, which is typically classified by the amount of impurities such as oxygen and iron [13]. A representative Ti alloy of particular interest is Ti-6Al-4 V, which is considered the "workhorse" among α/β Ti-alloys [14,15].

1.2. Hydriding in Ti

Despite the general corrosion resistance, there is a major concern associated with hydrogen or hydride phases residing in the Ti alloy matrix. Historically, this has led to issues with environmentally assisted cracking, including hydrogen embrittlement (HE) and hydride-induced cracking (HIC) [5,16]. Specifically, titanium hydride in the form of TiH_x ($0 < x \leq 2$) often precipitates at the matrix surface and in the bulk material in application environments featuring H_2 gas, atomic H, or H^+ [17–21], which can eventually induce crack initiation and mechanical failure as the lattice deforms and stress accumulates [22,23]. Hydride formation can also be induced by an electrochemical process, which involves oxidation of Ti and reduction of H^+ (proton) or atomic H [17–20,24,25]. Externally applied tensile loads and residual stresses promote ingress of hydrogen into the Ti matrix, eventually inducing embrittlement, with cracks preferentially propagating along phase boundaries or directly across matrix grains [7]. Hydrides can also play a role in the corrosion susceptibility of Ti and Ti alloys, either acting as a protective barrier on the matrix surface inhibiting corrosion attack [17,26] or assisting crevice corrosion and stress-induced corrosion cracking at local microstructural defects such as inclusions and phase interfaces [7,27].

In the past few decades, there have been significant efforts to better understand the physicochemical phenomena underlying Ti hydrogenation, including H adsorption, transport, and hydride phase formation, as well as their impact on the mechanical, microstructural, and corrosion properties of base materials [5,17–20,23–35]. Broadly speaking, these

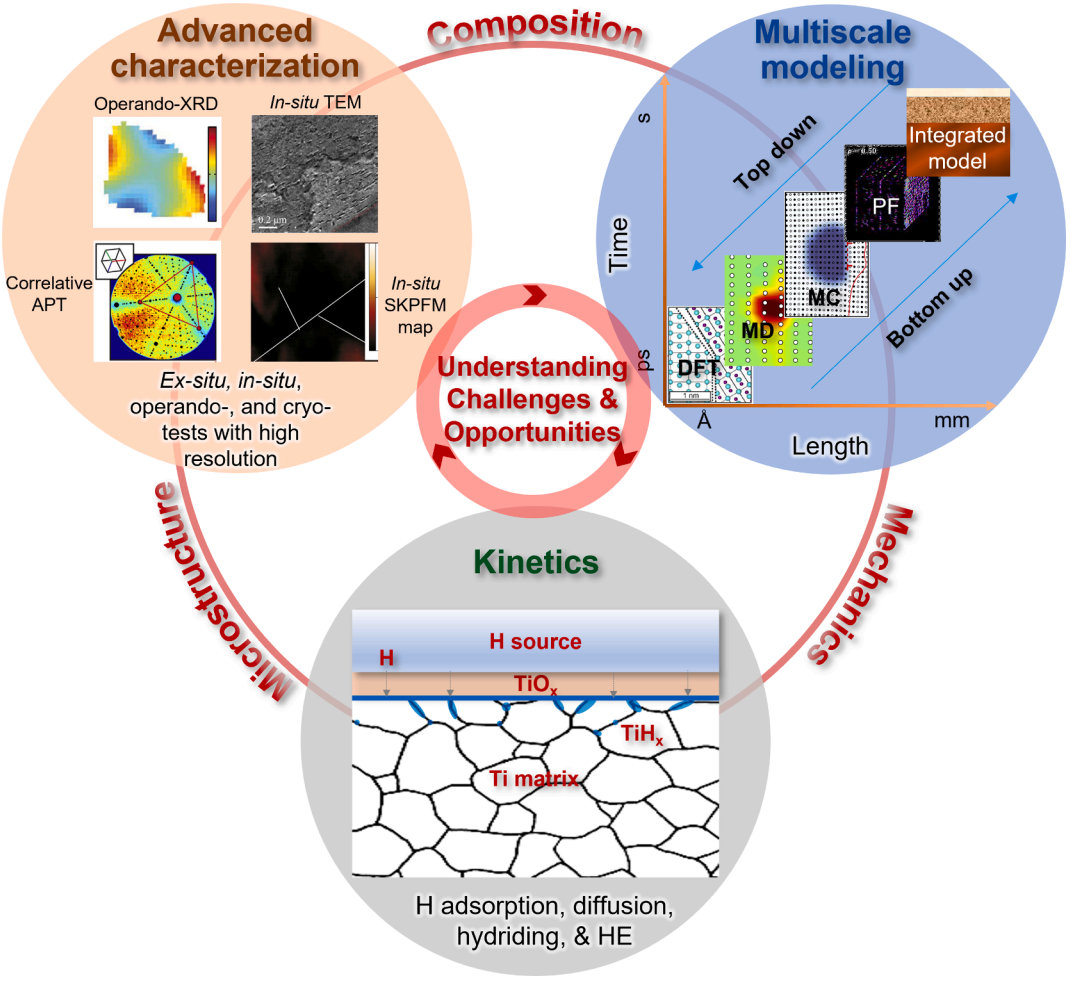

Fig. 1. Schematic synopsis of the current perspective, illustrating the integration of advanced characterization, multiscale modeling, and kinetic testing to understand hydriding phenomena in Ti. Examples of advanced characterization include: operando XRD imaging of strain evolution during H-charging in Pd (red indicates higher strain), correlative-APT analysis of hydrided Ti-2wt.%Fe sample, *in situ* TEM snapshots of Ti-0.1O sample during heat, and *in situ* SKPFM potential mapping of steel during H-charging (dark contrast indicates more H and white lines represent grain boundaries), sourced with reuse permission from references [36,33] (© 2018 Acta Materialia Inc. Published by Elsevier Ltd.), [35] (Published by Elsevier Ltd on behalf of Acta Materialia Inc.), and [40] (Copyright © 2011 Elsevier B.V.) respectively. Examples of multiscale modeling include: atomic modeling of α-Ti/hydride interface, MD modeling of edge dislocation core of Ni metal, MC modeling of H distribution along Ni, and PF simulated δ-hydride formation in bi-crystal grain boundaries in α-Zr, sourced from references [33,48] (Copyright © 2016 Acta Materialia Inc. Published by Elsevier Ltd.), [49] (Copyright © 2015 Acta Materialia Inc. Published by Elsevier Ltd.), and [50] (© 2019 Acta Materialia Inc. Published by Elsevier Ltd.), respectively.

Table 1
Identified key challenges associated with hydriding phenomena in Ti metal/alloys.

Category	Challenges and/or gaps
Influence of metal properties	1. The dependence of hydrogen permeation on the structural and compositional features of the native Ti oxide film is not well understood.
Critical conditions for H uptake	2. Existing results have been inconclusive with respect to the impact of defects (impurities and phase/grain boundaries etc.) on H transport and hydriding in Ti. 3. Environmental factors affect the critical conditions for H uptake. It is challenging to quantitatively compare H uptake, hydrogen/hydride content, and distribution under different charging environments.
H–defect interaction and hydride formation	4. Contamination in sample preparation complicates precise quantification of hydrogen/hydride content and distribution. 5. Complex H–defect interactions (e.g., with dislocation network/clusters, stacking faults, interfacial/phase boundaries, and impurities) challenge reliable experimental and modeling descriptions and their multi-scale integration for studying hydrogenation.
Mechanical response of H incorporation and/or hydride formation	6. Intrinsic mechanical properties of Ti hydrides are critical for understanding matrix embrittlement and cracking, but specific mechanical influences of H incorporation are difficult to discern experimentally. 7. High spatial and temporal resolution studies are necessary to understand the highly dynamic evolution of lattice deformation, local strain and mechanical response (e.g., cracking) due to the high mobility of H and the small length scales involved.

studies fall within five major categories based on the phenomenon of interest, as illustrated in Fig. 1: (1) the effect of surface oxide on H adsorption and transport; (2) the effect of Ti matrix integrity (embrittling species, roughness, surface treatment/residual stress, and microstructure) on H transport and hydriding; (3) the effect of hydride formation on embrittlement and localized corrosion resistance; (4) relevant technique development based on high-resolution, *ex situ*, *operando*, and *in situ* probes, as well as cryo-methods for local structural, chemical, and electrochemical analysis; (5) multi-scale modeling ranging from atomic to continuum scale.

1.3. Perspective synopsis

Recent research advances in Ti hydriding phenomena have been driven by increasingly mature and emerging experimental characterization tools (see Fig. 1) including, but not limited to: *in operando* X-ray diffraction (XRD) and imaging [36,37], atom probe tomography (APT) [33,34], *in situ* atomic force microscopy/scanning Kelvin probe (AFM/SKP) [38,39 40–46], *in situ* scanning and/or transmission electron microscopy (S/TEM) [24,35], and cryo-controlled characterizations [34]. Meanwhile, the fundamental understanding of hydriding has been catalyzed by progress in modeling efforts from atomistic to continuum scale with significantly improved computational capabilities (Fig. 1): density functional theory (DFT) calculations [32,33,47], molecular dynamics (MD) [18,48], Monte Carlo (MC) [48,49], phase-fielding modeling (PFM) [8,15,50], and integrated models [21,51–53] that transcend idealized representations. However, a number of knowledge gaps and challenges, some of which are listed in Section 1 (Table 1) and will be discussed in detail in Section 2, remain at different length scales. In our view, tighter integration of experimental and modeling research, either through a validation feedback cycle or direct comparison, is sorely needed to form a comprehensive story of Ti hydriding phenomena and to resolve these remaining challenges.

This work is intended to briefly review the recent advances in characterization and modeling efforts for investigating a variety of fundamental chemical, physical, and materials processes associated with Ti hydriding, as well as how these phenomena are coupled. In particular, we focus on how such experimental and modeling efforts have been applied to shed light on key identified challenges. Finally, we propose new perspectives on how advanced characterization and multiscale modeling could be more effectively integrated to bridge remaining knowledge gaps, as illustrated schematically in Fig. 1.

2. Recent advances and key challenges

2.1. Chemistry and composition

2.1.1. Hydrogen uptake

There are three methods reported in the literature for charging H into the Ti matrix, namely, electrochemical charging, gaseous charging, and H ion irradiation. The first two are the most frequently used. Here the mechanisms of these methods are briefly introduced, and their advantages and disadvantages are discussed.

2.1.1.1. Electrochemical charging. In the electrochemical charging method, TiH_x formation can occur in Ti metals/alloys via corrosion processes in acidic or deaerated aqueous environments. In these processes, H adsorption is readily accessible from cathodic discharge of H^+—i.e., cathodic galvanostatic or potentiostatic polarization or by interfacing Ti with a more galvanic metal [7,17,18,26,27,54–58]. Further penetration through the outer oxide film into the alloy matrix involves coupled processes of additional hydrogen absorption and redox chemistry, which are generalized in equation (1):

$$TiO_2 + xH^+ + xe^- \rightarrow (Ti^{IV})_{(1-x)}\,(Ti^{III})_xO_{(2-x)}\,(OH)_x \quad (1).$$

Experimental observations demonstrate that H absorption through intact TiO_2 films into Ti becomes efficient at a cathodic potential range around –0.6 to –1 V_{SCE} [18,56]. The resulting TiH_x composition varies depending on values of the cathodic charging current densities and/or charging potential [17]. Notably, defects can aid hydrogen permeation through the oxide film, for example via the weak points associated with structural defects including oxygen vacancies, grain boundaries and triple junctions in polycrystalline oxides, and lower-density regions associated with amorphous oxides or porosity; in such cases, the required cathodic potential for penetration can be less negative, e.g., $\sim -0.35\ V_{SCE}$ [18,28]. External stress also introduces defects in the oxide film and matrix that eventually lead to less negative cathodic potentials for H charging [7,57]. Accordingly, Ti hydrides formed on Ti metal surfaces have been shown to be unevenly distributed, and preferentially located at intermetallics and grain boundaries [58]. As another strategy to avoid the oxide-induced impedance, Abul-Hamid and Latanision removed the oxide surface layer and coated the underlying Ti metal with palladium prior to electrochemical charging [59].

2.1.1.2. Gaseous charging. Gaseous hydrogenation is usually performed at elevated temperatures with a typical range of 480 °C to 650 °C, and under gas environments of pure H_2 or H_2 mixed with inert gases (e.g., N_2 or Ar) at typical pressures of 1 atm [60–64]. Occasionally, much higher pressures (e.g., from a few atm to 100 atm) are used for fast charging, which easily leads to surface and subsurface cracking. The charging process involves the dissociation of H_2 gas molecules, surface adsorption of H, and subsequent incorporation into the metal/alloy matrix. As in electrochemical charging, incorporation requires that the adsorbed H atoms first penetrate through the surface oxide film. The typical hydrogen concentration usually spans from a couple hundred weight part per million (wppm) to several thousand wppm for complete hydriding before the samples break into pieces. Note that the amount of gaseous charged hydrogen that can be incorporated is not restricted by the terminal solid solubility (TSS) [65] of hydrogen in the alloy matrix. The TSS of hydrogen is an important parameter in hydride-forming metal alloys and increases with temperature. If this solubility is exceeded, it can make the metal and alloys susceptible to hydride-induced cracking. Another concern is the microstructure evolution during gaseous hydrogen charging at elevated temperature, which is a concurrent process that is coupled to hydrogenation.

2.1.1.3. Ion implantation. Ion implantation is a powerful method that has been frequently adopted to modify material chemical, mechanical, or electrical properties [66–71]. Although less common than electrochemical or gaseous charging, it has been used to implant H ions into the Ti matrix to study hydriding behavior [67–69]. The average penetration depth of ions is usually in the range of nanometers to a few micrometers. Therefore, ion implantation is particularly powerful for studying hydriding in the near-surface domain. However, the major concern with ion implantation is the irradiation damage that is transferred to the matrix due to the need to accelerate the implanting ions for entry. During this process, the accelerated ions transfer their kinetic energy and momentum to the electrons and nuclei of the target atoms and generate a significant fraction of defects, such as atom vacancies or ion interstitials [69]. Relevant research [67–69] on Ti hydriding has confirmed that the major defects generated by ion implantation were near the target material surface, and that the implanted hydrogen ions were mostly trapped at these defects.

2.1.1.4. Comparison and discussion. Although electrochemical charging, gaseous charging, and ion implantation for hydrogen share some similarities (e.g., hydrogen adsorption, penetration through the oxide film, hydride formation, as well as coupling of these processes to defects) [72,73], datasets collected using different methods should not necessarily be interpreted in the same way. This is mainly because the driving forces and associated mechanisms differ across the three methods: electrochemical potential/current for electrochemical charging, temperature and pressure for gaseous charging, and irradiative damage for ion implantation.

Electrochemical charging usually develops a much higher hydrogen partial pressure (e.g., on the order of 100 atm or higher at the metal-liquid interface [72]), which leads to the amount of absorbed hydrogen in the Ti surface region being significantly higher. However, unlike gaseous charging, the amount of hydrogen electrochemically charged into the matrix is limited by the TSS of hydrogen in that matrix [73], which means hydrogen diffusion and hydriding kinetics in the subsurface are usually limited by the ambient charging temperature (<100 °C). Another difference is that electrochemical charging often induces a highly hydroxylated surface due to the abundance of water, leading to fundamentally different surface processes. In addition, because of its much higher temperature range (480–650 °C) and sometimes high H_2 partial pressure, gaseous hydrogenation can penetrate the surface oxide rapidly and crack the surface. The higher temperatures for gaseous charging can also lead to microstructural evolution of the matrix due to an annealing effect, which is a concurrent process with hydrogenation. Ion implantation adds the factor of irradiation damage to the hydrogenation layer and matrix by introducing a significant amount of microstructural and point defects, including vacancies and cation interstitials. The hydriding layer in this case is also usually limited by a short implantation depth range of nanometers to a few micrometers.

For all three charging modes, the exposure times and resulting hydrogen concentration gradients can also introduce additional complexities. In particular, the nature of the surface oxides (e.g., thickness and composition) changes as a function of charging time, so the uptake behavior is rarely uniform. Moreover, the time required for complete hydrogen penetration and dissipation of intrinsic hydrogen concentration gradients in Ti depends on the specimen size and can be limited by the continual accumulation of near-surface hydrogen and hydrides. Such accumulation can impede diffusion of hydrogen and promote additional steep concentration gradients between sample surface and center.

For the reasons stated above, a direct comparison between the three methodologies is not straightforward. Accordingly, development of models that represent these three methods should take in to account the different physical and chemical phenomena that govern hydrogen uptake in each case. In addition, the following efforts towards more systematic and reliable comparisons across different charging methods are suggested: 1) use a readily accessible pseudo reference material, such as a single crystal, that can be used by different researchers to minimize the effects of individual materials properties on charging behavior; 2) explicitly specify the charging method and strictly control and report charging parameters to ensure repeatability and reproducibility; 3) develop proper analysis protocols that can eventually be published as "standard or gold" rules for certain standard alloys or pseudo reference materials, such as a standard protocol for TDS measurement.

Table 2
Representative hydrogen diffusion coefficients in Ti oxide, Ti matrix, and Ti grain boundaries based on experimental measurements.

Materials or features	Diffusion coefficient, $cm^2\ s^{-1}$	Reference
Single crystal rutile	7.5×10^{-20}	[76]
	$10^{-11} - 10^{-13}$	[85]
Polycrystal rutile thin film	2.9×10^{-20}	[77]
Polycrystal anatase thin film	4×10^{-15}	[80]
Amorphous TiO_2 thin film	1×10^{-15}	[80]
	$10^{-18} - 10^{-17}$	[28]
a-Ti matrix	2.6×10^{-10}	[86]
β-Ti matrix	$\sim 5 \times 10^{-9}$	[87]
Grain boundary in pure Ti matrix	9.1×10^{-5}	[59]

2.1.2. Hydrogen transport through oxide surface layers

The surface Ti oxide film can exist in either a crystalline (typically anatase and/or rutile) or a noncrystalline form, or else as a mixture of the two. This surface oxide layer acts as a robust barrier layer that protects the Ti matrix from H ingress [74,75], significantly slowing down the hydrogen diffusion rate. As summarized in Table 2, an apparent hydrogen diffusion coefficient was reported in the range of 10^{-18}-10^{-15} cm^2 s^{-1} in amorphous TiO_2 thin films [28,76] and around 2.9 × 10^{-20} in rutile thin films [77]. In bulk TiO_2, a H diffusion coefficient was estimated around 5.3 × 10^{-16} cm^2 s^{-1} at ambient temperature, based on experimental measurements on single-crystal rutile [76]; a similar diffusion coefficient of 2.84 × 10^{-16} cm^2 s^{-1} at 373 K was found for oxides covering pure α-Ti metal [78].

The hydrogen barrier efficacy of Ti oxides strongly depends on the oxide structure and composition [55,79]. Structural defects such as vacancies, grain boundaries, and triple junctions at the Ti surface, as well as chemical heterogeneities such as cathodic intermetallic compounds (e.g., Ti-Pd) can significantly impact hydrogen transport [13]. In general, faster H diffusion is expected in amorphous or polycrystalline TiO_2 than in single-crystal TiO_2 considering the structural and chemical defects in the former. However, the existing data is not always consistent with this notion. For example, a recent study reported a much higher apparent H diffusion coefficient of 10^{-15} $cm^2 \cdot s^{-1}$ that was similar in both amorphous and amorphous/anatase mixed oxide films [80]. This discrepancy is likely due to porosity in their column structure contributing to the fast diffusion, which renders the amorphous and partially crystalline samples indistinguishable.

Moreover, the H-charging process itself can lead to concurrent compositional, structural, and electronic changes in the surface oxides, which in turn can influence H transport and trapping in the oxides and the underlying matrix metal as the reaction proceeds. Hannula et al. [81] recently indicated that atomic H treatment of deposited TiO_2 (at 300 °C in UHV chamber) created an electronically "leaky" and photoelectrochemically unstable film due to the formation of O vacancies and TiO_2 dissociation. This "leaky" phenomenon, which signals a change in electronic structure, should be heeded during routine hydrogen charging of the Ti oxide surface and subsequent analysis.

In parallel with the experimental work, computational studies based on first-principles DFT calculations have been carried out to investigate the mechanism of hydrogen transport in Ti oxides. These studies have largely focused on crystalline systems with specific orientations; nevertheless, several important findings have been reported. Specifically, H migration from surface to subsurface sites in anatase has a lower kinetic barrier than that of H_2 desorption, which indicates that H likely preferentially diffuses to the subsurface and further transports into the bulk [82,83]. In addition, subsurface oxygen vacancies can favorably accommodate H [82,83], and preexisting atomic H in the oxides enhances H diffusion into the subsurface while simultaneously preventing the escape of H [84].

Collectively, these studies not only provide a detailed understanding of hydrogen transport in the oxide, but also suggest a possible strategy to enhance the hydrogen storage capability of the material. Nevertheless, given that H diffusion data are inconsistent, and that the specific connection to structural and compositional complexities in TiO_2 are not well established, much remains to be understood regarding the mechanism and degree to which the Ti oxide film can act as a hydrogen barrier. Approaches to precisely predict hydrogen transport through the oxide and its potential interaction with specific heterogeneities within the oxide are particularly needed.

2.1.3. Hydrogen transport and trapping in Ti

Following surface oxide permeation, H can be transported, redistributed, and/or trapped within the Ti matrix. H transport in Ti usually occurs via three pathways: short-circuit transport via lattice defects, dislocation movement, and diffusion along grain boundaries. It was reported that for the pure Ti matrix, the effective diffusion coefficient of H along grain boundaries is around 9.1 × 10^{-5} cm^2 s^{-1} [59] (Table 2) - significantly higher than the H transport within the grain lattice (e.g., 2.6 × 10^{-10} cm^2 s^{-1} in CP α -Ti grains [86]).

Compared to the Ti matrix, the diffusion kinetics in the hydride layer are reported to be about two orders of magnitude slower than in the Ti matrix, around 4x10^{-12} cm^2 s^{-1} at room temperature [28,88]. This is in general agreement with extrapolations from first principles [89]. Once the hydride forms near the Ti surface due to continuous H adsorption, further H ingress into the metal would therefore be significantly inhibited. In addition, the H diffusion coefficient in the hydride further decreases with increasing content of H in Ti hydride [87].

H transport can also be inhibited by irreversible trapping, for instance at various types of matrix defects (e.g., dislocations, precipitates, and grain boundaries). In principle, the concentration of trapped H, as well as the associated binding energies at trapping sites, can be deduced through relevant calculations and analysis of adsorption/desorption profiles [90,91]. Section 2.2 provides a more complete discussion of defect interactions with H. In addition to the specific connection between these defects and hydrogen trapping in Ti metal and Ti-based alloys [91], insights may be gleaned from analogous studies on various steels. For instance, several trapping energies (0.14, 0.11, 0.27 and 0.54 eV) corresponding to different peaks in the thermal desorption spectra of H have been reported for martensitic steel. These values of trapping energy are comparable to those reported for other tempered martensite (0.15 and 0.68 eV) [92], pure iron (0.17, 0.35, 0.60 eV) [93,94], and low-carbon steel (0.13, 0.24 and 0.50 eV) [95] samples. The consistency among these independent reports suggests that H is preferentially trapped in the same types of trapping sites with comparable trapping energies. These trapping energies from low to high are associated respectively with interstitial sites (energy of −0.16 eV) [93], reversible trapping sites (-0.29 eV) related to elastic field near-edge dislocations [90,94] or to semi-coherent precipitates [90,96,97], and irreversible trapping sites (-0.59 eV) related to dislocation cores [98].

2.2. Microstructure phenomena

2.2.1. H-dislocation interaction

When H concentrates around dislocations in metals, it impacts the interactions between these dislocations and other dislocations/defects and can eventually lead to local plasticity, with impacts similar to macroscopic brittle fracture. Whereas the nature of hydrogen-dislocation interactions has been extensively studied in BCC metals, there have been far fewer relevant studies in HCP metals such as Ti. It is often supposed that hydrogen affects dislocation mobility via the kink-pair nucleation and migration mechanism [99–102]. Low concentrations of hydrogen (e.g., 0.1 atom ppm) enhance dislocation mobility by promoting kink-pair nucleation whereas high concentrations of hydrogen (e.g., 10 atom ppm) decrease dislocation mobility by impeding kink-pair migration [102]. Note that mobility of screw dislocations is much lower than edge dislocations, so plasticity is majorly limited by the former in bcc metals [103]; however, the relevant reports of hydrogen-dislocation interaction in HCP metals are very limited [99–102]. The impact of hydrogen on dislocation mobility has also been discussed in the context of the hydrogen-enhanced local plasticity (HELP) mechanism on local hydrogen-dislocation interactions [48]. Within HELP, the movement of hydrogen clouds around dislocations follows the movement of the dislocations during plastic deformation, and HE is largely determined by the H-dislocation interactions via the population of free electrons in the hydrogen clouds [91].

To reveal these linkages, advances have consistently been made both experimentally and theoretically on the quantification of H concentration and dislocation interactions in various HE-sensitive metals, inlcuding Ti alloys [29,30,32,48,49,89,104–120]. From the experimental side, attempts to link local H-dislocation interactions to microscopic embrittlement in Ti could benefit from more detailed studies of H in other metal alloys using advanced techniques. For example, the series

of works on Ni and steel HE reported by Barnoush et al. [105–107,111,118] using the *in situ* electrochemical nanoindentation (ECNI) method falls within the category of nanometer-to-micro-scale examination of both H-defect interactions and mechanical responses. Quantitative *in situ* TEM nanomechanical characterization could likewise provide key insights, as utilized by Zhu et al. [110] in a pioneering study on local H-dislocation interactions at free metal nanowire surfaces, which reported hydrogen-induced suppression of dislocation nucleation, contrary to the well-reported hydrogen-induced promotion of such nucleation in many bulk metals. Note these most other investigations of H-defect interactions (e.g., with vacancies, dislocations, grain boundaries, or intermetallics) have relied on macroscopic testing [113,114,117,121,122], which normally combines effects of multiple defects with different length scales. The challenge remains to separate the intrinsic impact of dislocations from other defects, such as twinning nucleation and stacking faults, on hydriding behavior.

Ab initio simulations based upon DFT can provide a reliable computational tool to quantitatively evaluate the energetics of defect interactions during the Ti hydriding processes [123,124]. However, complex defects such as dislocation networks or clusters, as well as stacking faults and interafacial/phase boundaries, feature large strain fields that are often difficult to address with DFT alone. Classical molecular dynamics simulations are one alternative, but it is difficult to validate reliable interatomic potentials for defect interactions in the Ti-H system [89], which affects predictions of hydrogenation phenomena. For example, the inconsistency between classical molecular dynamics and ab initio simulations for H diffusion in Ti hydride was found to most likely be due to the Ti-H interatomic potential [112]. Beyond this, the materials in service are often under external load, which concentrates stresses that can facilitate H transport and lead to local buildup of H, promoting dislocation nucleation. Such mechanisms are common in metals and add to the difficulty with modeling these systems, typically requiring integration of models at different length scales.

Overall, despite advances in understanding, robust quantitative descriptions of localized H at or near dislocations and their specific linkage to the microscopic/macroscopic brittleness of the Ti matrix are still lacking. Associated questions remaining to be answered are: what is the local H content near dislocations? What is the strength of the H-dislocation interaction and how can the dislocation interaction be deconvoluted from that of other defects? How do the interactions impact local hydride formation and plasticity and further link to macroscopic mechanical reponse, including brittleness? Closer feedback between multiscale modeling and experimetal investigations, which provide complementary benefits and liabilities, may provide a more suitable approach to isolate specific H-dislocation interactions and trace their impacts across scales in hydride-forming materials.

2.2.2. H-grain/phase boundary interaction

In addition to its interaction with dislocations, H can also impact Ti properties by interacting with grain boundaries. A few studies have been carried out at atomic level on the hydrogen impact on the mobility of twin boundaries (TB) in Ti, e.g., (112 $\bar{1}$) [125]. These studies confirm that the (112 $\bar{1}$) TB glides easily and would readily encounter the mobile H atoms [126]. Note also that the energy barrier for TB shifting increases gradually with increasing hydrogen concentration. Unfortunately, such studies remain limited, and information regarding the interaction of H with other grain boundary orientations is sorely needed.

Literature reports also indicate that grain boundaries and phase boundaries in Ti can act as preferential nucleation sites for growth of hydrides [127,128]. There have been additional reports exhibiting a high fraction of intragranular hydrides found in matrices even with relatively large grains [24,129]. For example, the nucleation and growth of $TiH_{1.5}$ hydride in Ti64 initially occurred in the β phase because of the high diffusivity and contiguity of H in this phase [30,31]. In such instances, the process is accompanied by local stress accumulation and H confinement near the alpha/beta boundary, which eventually leads to hydride formation preferentially along the boundary. Such studies highlight the complex interaction between atomic disorder, stress, and composition at phase and grain boundaries, which remains difficult to unravel with most current approaches.

2.2.3. H-impurities/inclusions interaction

There are several major metallic impurities in CP Ti, such as Fe, Pd, and Ni, that may influence the hydrogenation of Ti because they are H sensitive. Fe is the most common impurity and present in many grades of CP Ti [130]. Pd is usually present in multi-grades of CP Ti metals such as Grades 7, 16, 18, and 24 [131], and Ni is usually found in CP Ti metal Grade 12 [131]. These elements usually dissolve in the solid solution of Ti, either in the α-phase, the β-phase, or at the α/β interface. Their solubility tends to be higher in the β-phase than in the α-phase due to their affinity and stability in the BCC structure. In fact, these metallic impurities prefer to incorporate substitutionally as stabilizers in β-Ti regardless of their atomic size or chemistry [132]. However, when the impurity content exceeds their solubility in the Ti solid solution, they tend to precipitate to form Ti-R (R = Fe, Pd, or Ni) intermetallic compounds such as TiFe and Ti_2Fe [133], TiPd and Ti_2Pd [134–138], and Ti_2Ni [13,139,140], further complicating the hydriding mechanism. For example, Ti-Fe particles can precipitate even if the Fe impurity concentration is as low as ~ 0.03 wt% [130].

Extensive research regarding the influence of the elemental impurities (Fe [27,58,59,141–143], Pd [144,145], and Ni [13,139]) on hydrogen adsorption/absorption, hydrogen transport (diffusion and penetration), and hydriding has been carried out. However, the findings are often inconclusive or contradictory. Some studies reported that enriched elemental impurities in Ti solid solutions provide an entry point for hydrogen to the underlying Ti metal and promote hydrogen adsorption/absorption and hydrogen transport [139,144,146]. However, other studies determined that hydrogen incorporation and transport efficiency decreased with the rise in elemental impurity content in Ti [141,145]. For example, Cotton [146] reported that diffusion rate was proportional to the concentration of elemental Fe, and that hydriding was promoted by elemental Fe impurities. However, Covington [141] demonstrated that less hydrogen was absorbed as the Fe content increased and indicated that low levels of Fe in Ti do not make it more susceptible to hydriding.

The impact of Ti-R intermetallic compounds on hydriding phenomena have also been investigated. Ti-Fe particles can impede hydrogen absorption and diffusion because hydride formation in/around Ti-Fe particles usually causes less lattice distortion than in Ti solid solutions [147]. Along these lines, Yan et al. [27] found that the hydrogen penetration depth into the matrix decreased with the presence of Ti-Fe particles. Liu et al. [17] reported preferential H aggregation at Fe-containing particles along grain boundaries in CP Ti-2, which might be due to either enhanced H diffusion or preferential formation of hydrides. Grade 16 CP Ti was shown to be more resistant to hydride formation and HIC than Grade 2 CP Ti and 12104–105 Ti due to the presence of Pd-Ti particles in Grade 16 and the high solubility of H in these Ti-Pd intermetallic compounds, which act as a H sink [134,135]. Authors of these works further stated that the Ti-Pd compounds themselves do not provide an entrance for H absorption but rather catalyze proton reduction and hydrogen evolution, which apparently contradicts with the high solubility of H in Ti-Pd particles and with Pd content promoting H adsorption [134–140]. Hydrogen adsorption can also be promoted by the β-phase of Ti as it is usually rich in impurities and can be considered as an impurity-containing intermetallic compound. The β-phase usually distributes discontinuously along grain boundaries in CP Ti and can form a continuous network in (α + β) Ti that acts as a fast diffusion pathway for H [13,139].

The enrichment and distribution of Pd, Ni and Fe can clearly have a significant influence on the hydrogen adsorption, penetration, and hydriding behavior of Ti. However, the conflicting nature of some of the

literature reports, as well as a lack of understanding of key mechanistic details, prompt additional investigation. Critical information is missing to thoroughly understand the role of these elemental or particle impurities in hydrogen adsorption, transport, and hydride formation. Research efforts to reveal the decoupled effects on each of these processes is particularly important not only for Ti, but also for other hydrogen-sensitive metals, e.g., Zr and Al [148–150]. Note that non-metallic impurities e.g., C, O, and N are not discussed here, but it is helpful to realize that these impurities can also compete with H adsorption within Ti matrix [151], particularly at defects that also function as H sinks.

2.2.4. Hydride nucleation and growth

Hydride formation and the resulting composition are also strongly dependent on microstructural features. In general, three types of Ti hydrides with different compositions and crystal structures are consistently reported: face-centered tetragonal (FCT) ε-hydride (TiH_2, c/a < 1); stable face-centered cubic (FCC) δ-hydride (TiH_x, $1.5 < x < 1.99$); and metastable FCT γ-hydride (TiH, c/a > 1) [24,152,153]. The lowest-stoichiometry hydride was reported to be $TiH_{(0.17\text{-}0.2)}$ with a lattice parameter a of 4.40 Å, formed in α-Ti [19,154]. At lower concentrations, H remains in α-Ti with no hydride precipitate. The δ-phase hydride has been the most frequently observed Ti hydride. Hydrides grown under galvanostatic conditions, regardless of variation in charging durations or charging current densities, primarily consisted of $TiH_{1.5}$ (δ-hydride) with a minor fraction of $TiH_{1.7}$ and TiH_2 [17]. The preferential formation of δ -hydride has been attributed to the relatively small misfit strain at the δ hydride/matrix interface [155], close-packed substrate textures for both δ -hydride and α -matrix [156,157], preferential co-existence of solid solutions of both the δ -hydride and α -matrix phases [127,158], and preferred orientation of δ -hydride (200) along Ti (002) [34,127]. Formation of plate-shaped or lath δ-hydride was also confirmed in α/β Ti-55 alloys [159].

It has been reported that hydride nucleation in Ti matrix usually follows four different orientations, as tabulated in Table 3 [24,152,153]. Among these, two of the most frequent orientations (ORs) are OR1 and OR2 for the α-Ti/δ-hydride transition[160]. Details of ORs between hydrides and the Ti matrix have been documented elsewhere [24,152,153]. Nevertheless, the specific impacts of evolving strain, dislocation density, composition, interfacial coherency, and similar factors on hydride nucleation probability and preferred ORs have eluded detailed investigation.

Experimentally, one challenge in addressing key unknowns regarding hydride nucleation is the sensitivity of conclusions to sample preparation. Hydride formation can readily occur even from sample grinding and polishing, which complicates interpretation. In particular, Ti hydride nucleation and phase transformation are commonly identified in the process of thin sample fabrication using focused ion beams (FIB) and in subsequent TEM analysis [34,35]. For example, the conventional FIB-liftout process often induces δ- and/or γ-hydrides [35,161]. It has been further demonstrated that FIB-induced Ti hydrides do not precipitate within grains but rather preferentially form along α -phase grain boundaries and along α /β phase boundaries [33]. The temperature of sample preparation also plays a critical role, as no hydride formation was observed in cryo-plasma-FIB-prepared samples [34]. On the other hand, thermally produced FCC Ti-X phases are closely related to contamination by oxygen in high-purity Ti thin samples based on *in situ* TEM heating studies at ~ 600 °C [35,162], likely with analogous effects for hydride formation. Zr has a similar concern of contamination during sample preparation [163,164]. Sample handling is likewise critical because exposure to air can result in H contamination in the form of moisture [165]. To minimize H (and also O) commination, Breen et al. [166] performed all transfers and APT analysis under vacuum and cryogenic conditions. Such cryogenic conditions served two purposes: (1) to slow out-diffusion of H from the sample; and (2) to reduce background H by removing water vapor, which is often a major component of residual gas in vacuum chambers.

Table 3
Four orientation relationships of α-Ti / δ-hydride transition.

Orientation relationship		Interface plane
OR1	$\{0001\}_\alpha$ // $\{1\,\bar{1}\,1\}_\delta$, $<1\,\bar{2}10>_\alpha$ // $\langle 1\,1\,0\rangle_\delta$	$\{10\,\bar{1}\,3\}_\alpha$ // $\{1\,\bar{1}\,0\}_\delta$
OR2	$\{0001\}_\alpha$ // $\{0\,0\,1\}_\delta$, $<1\,\bar{2}10>_\alpha$ // $\langle 1\,1\,0\rangle_\delta$	$\{10\,\bar{1}\,0\}_\alpha$ // $\{1\,\bar{1}\,0\}_\delta$
OR3	$\{10.11\}_\alpha$ // $\{1\,\bar{1}\,1\}_\delta$, $<1\,\bar{2}10>_\alpha$ // $\langle 1\,1\,0\rangle_\delta$	$\{0001\}_\alpha$ // $\{1\,\bar{1}\,2\}_\delta$
OR4	$\{\bar{1}\,011\}_\alpha$ // $\{0\,0\,1\}_\delta$, $<1\,\bar{2}10>_\alpha$ // $\langle 1\,1\,0\rangle_\delta$	$\{10\,\bar{1}\,1\}_\alpha$ // $\{1\,\bar{1}\bar{1}\}_\delta$

2.3. Mechanical performance & testing

2.3.1. Mechanical properties of Ti hydrides

The mechanical behavior of hydrides is complex: the deformation and brittleness of hydrides are determined by the hydride distribution, morphology, size, and orientation, as well as environmental factors such as temperature and applied stress [22,47,167–174]. Acquiring a thorough understanding of these intrinsic mechanical properties and their dependencies on materials features and environmental conditions is critical to discern potential impacts on HE and HIC tendency. Although some hydride mechanical property data have been documented in literature [32,47,172,174], reports are still very limited, particularly from detailed experiments [167,174]. Some existing data regarding the mechanical properties of hydrides, including fracture toughness (K), elastic modulus (E), bulk modulus (B), and shear modulus (G), are summarized in Table 4.

The fracture toughness of hydrides, for example, has been studied only for the δ-phase ($TiH_{1.6}$) using bending experiments, and it was reported to be around 2.2 MPa*$m^{1/2}$ [167]. This is a common value for ceramics but significantly below the value of 50–70 MPa*$m^{1/2}$ reported for the metallic matrix α-Ti [168]. The fracture toughness of the hydrides was calculated to be 0.7 and 0.4 MPa*$m^{1/2}$, respectively, for the δ-phase ($TiH_{1.5}$) and ε-phase (TiH_2) based on ab-initio calculations and Griffith-Irwin theory [32]. Note that the discrepancy between experimental observations and DFT calculations can be explained in part by temperature effects, given that the ground-state DFT calculations are performed at 0 K, whereas low temperature usually decreases toughness [169].

The difference in fracture toughness between the δ-phase ($TiH_{1.5}$) and ε-phase (TiH_2) correlates with the Young's modulus, which is about two times larger for the δ-phase (125 MPa*$m^{1/2}$ by experiment [174] and 151 MPa*$m^{1/2}$ by DFT [47]) than for the ε-phase (60.1 MPa*$m^{1/2}$ by DFT [47]). Note only one existing experimental dataset [174] that includes Young's modulus (125 MPa*$m^{1/2}$), bulk modulus (125 MPa*$m^{1/2}$), and shear modulus (43 MPa*$m^{1/2}$) has been reported for δ-hydride to date, and no experimental values for the other Ti-hydrides exist, highlighting the data scarcity of mechanical properties of Ti-hydrides.

2.3.2. Mechanical/stress response to hydride formation

Hydrogen incorporation into the Ti matrix causes lattice deformation, and further formation of Ti hydrides locally destroys the original matrix lattice. These structural changes are likely to contribute to the accumulation of volumetric and interfacial stresses, which can eventually lead to HE and/or HIC. Such effects have been observed in other hydriding-susceptible metals.

For example, H incorporation in Zircaloy-4 was found to induce significant strain in the δ lattice, leading to a transformation from the FCC δ-hydride to the HCP ζ-hydride (Zr_2H) [185]. Similarly, H charging in steel led to austenite phase peak splitting and the development of heterogeneous tensile strains on the basis of synchrotron grazing-incidence X-ray diffraction (GIXRD) studies [186]. Nevertheless, the specific connection between stress and hydride formation in the case of Ti derivatives is not entirely clear. For instance, J. Wen et al. [128], found that electrochemical H-charging in the β-21S Ti alloy over time did not lead to hydride nucleation even though a proportional increase

Table 4
Summary of experimental (Expt) and DFT calculated lattice parameters (in angstroms) and mechanical properties (in MPa*$m^{1/2}$) of Ti hydrides.

Hydride	Expt/DFT	a	c	E	B	G	K	Ref.
TiH	Expt	4.21	4.59					[158,175]
	DFT	4.168	4.584					[176]
	DFT	4.164	4.581	183	126	73		[177]
	DFT	4.171	4.581	85.5	129	31.7		[47]
$TiH_{1.5}$	Expt	4.40	4.40					[157]
	Expt	4.40	4.40	125	125	43	2.2	[167,178]
	DFT	4.360	4.404	187	130	74		[177]
	DFT	4.372	4.372					[179]
	DFT	4.355	4.394	151	137	57.5	0.72	[32,47]
TiH_2	Expt	4.53	4.28					[157]
	Expt	4.53	4.28					[180]
	DFT	4.513	4.179					[181]
	DFT	4.554	4.210					[182]
	DFT	4.532	4.187					[176]
	DFT	4.534	4.209		137	17.6		[183]
	DFT	4.517	4.201	121	139	45		[177]
	DFT	4.486	4.352					[184]
	DFT	4.527	4.199	60.1	141	21.1	0.43	[32,47]

in the lattice parameter of BCC β-Ti was observed.

We note that it can be difficult to experimentally reveal local mechanical responses to hydrogenation, in part due to the high mobility of H and the length scales associated with the strain. An efficient methodology to bridge this gap involves combining *in situ* nano-to-micron scale chemical and mechanical analysis with *in situ* hydrogen charging, which can eliminate the impact of hydrogen diffusion and loss during tests while simultaneously providing fundamental insights into local mechanical responses to hydrogenation with high resolution.

Meanwhile, these nano-to-micron scale experimental apparatus can provide useful measurements to compare to computational investigations at the atomic scale. For example, anisotropic strains associated with both OR1 and OR2 types (in Table 3) of hydride phase transformations have been modeled to reveal the orientation dependence [24]. The results show that for OR1-type δ-hydrides, the maximum and minimum transformation strains are achieved for directions along the $\{10\bar{1}2.6\}_\alpha$ and $\{0001\}_\alpha$ plane normals, respectively. In contrast, for OR2-type hydrides, the maximum (of 21.8%) and minimum strains are achieved for directions along the $\{10\bar{1}0\}_\alpha$ and $\{0001\}_\alpha$ plane normals, respectively. These findings suggest that grains with orientations that can more efficiently accomodate the strain associated with Ti-hydride transformation may also be more favorable for hydride formation. Further studies along these lines are recommended to reveal the full magnitude of the volumetric and interfacial stress effects on hydride formation and vice versa.

2.3.3. Hydride impact on general corrosion resistance

Similar to the functionality of the surface oxide film, the hydriding process creates a layer on Ti metal that ennobles the surface and is believed to provide some degree of corrosion inhibition [17,26,187]. For example, an increase in the average corrosion potential and decreased hydrogen discharge kinetics were reported for Ti metal and alloys upon surface hydride formation [17,26,58,188]. The increased corrosion potential is an indication of decreased overpotential for the cathodic hydrogen evolution reaction (HER) reaction and corresponds to the Ti corrosion rate. Ti was also found to be in the active dissolution state under reaction control prior to hydrogen charging, whereas a switch to the diffusion-controlled passivation state was observed upon growth of the hydride layer (also termed cathodic modification) [189].

A number of topics relating to the corrosion behavior of Ti metal and its alloys (including 3D printed Ti) have been reviewed recently, including general corrosion, methods for characterization Ti corrosion phenomena, passivation films, methods for corrosion mitigation, and the impacts of solution chemistry [26,190–195]. However, other important topics regarding the specific impacts of hydride formation on corrosion resistance have less extensively reported, such as the nature of the competitive growth and dissolution between oxide films and hydride films and its impact on surface protection, as well as the quantitative link between hydride microstructure (thickness, porosity, crystallinity, etc.) and corrosion resistance. In addition to experimental investigations, detailed multiscale modeling studies may provide further usefulness in this regard.

2.3.4. Hydrogen embrittlement without hydride formation

A significant amount of work has been dedicated to the mechanism of HE-induced failure in hydrogen-sensitive metals. Several possible HE mechanisms, including hydrogen-enhanced localized plasticity (HELP) [122,196–198], adsorption-induced dislocation emission (AIDE) [199,200], hydrogen-enhanced decohesion (HEDE) [201–203], and hydrogen-enhanced strain-induced vacancies (HESIV) [204–208], have been proposed in the past based on microscopic observations and modeling work. However, a general consensus regarding a single dominant mechanism by which hydrogen causes embrittlement has not been reached. More detailed discussions of HE mechanisms have been well documented elsewhere [91,109,122,196–200,204–208].

2.3.5. Hydride impact on localized stress corrosion cracking

Ti is sensitive to localized corrosion in an aqueous environment of low pH, high temperature, and/or high concentration of halides e.g., 0.5 wt% HCl or 1 wt% H_2SO_4 at 100 °C [209,210]. External mechanical loading or internal residual stress at localized corrosion sites further adds to the sensitivity of Ti to stress-assisted localized corrosion and cracking (SCC). Studying SCC under external stress loads is also practically relevant, as Ti alloys used as structural materials in a service environment must usually withstand external mechanical loading. Some recent progress and remaining issues regarding the mechanism of SCC under loading or at the crack tip as it pertains to hydride formation, hydrogen enrichment, or mixed oxygen/hydrogen enrichment are briefly discussed below.

Recent work has provided evidence that hydride formation itself can induce cracks, leading to mechanical failure in Ti alloys. Crack deflection and failure was observed in fatigue crack growth testing performed on Ti-10 V-2Fe-3Al alloys in high-pressure (8.3 MPa) H_2 gas [211]. The analysis revealed hydride-induced fatigue cracking, as TiH_2 was the dominant residual phase on the cracking surface. Furthermore, hydrogenation of the Ti β-phase was found to induce lattice deformation, introducing a localized stress field to the α/β boundary region that facilitated hydriding [31]. In this process, nanoscale cracks nucleated in the hydrides and propagated along the interface of the hydride with the β-phase, eventually leading to transgranular cracking across β grains. The large mismatch between the cracked β grains and the α grains also

ultimately resulted in transgranular cracking across the α grains. Adsorbed hydrogen can also chemically react with carbon at grain boundaries and produce methane gas, which can in turn lead to void formation and mechanical failure [212].

Nevertheless, hydride formation-aided SCC at a crack tip has been questioned in certain types of Ti alloys (e.g., Ti-4Al [30] and Ti-8Al-1Mo-1 V [213–216]) due to two aspects: the slow hydride formation kinetics and its orientation. On one hand, the onset of hydride nucleation was not observed in Ti-4Al until about 14 min after gaseous H_2 charging under a pressure of 16 kPa [215], which is indeed significantly slower than the crack propagation rate of around 10^{-5} m/s in an aqueous environment [214]. On the other hand, intergranular hydride formation was observed along phase (or grain) interfaces in Ti-811 in an aqueous NaCl solution around neutral pH; however, SCC fracture produced hydride-free intragranular facets across grains [215,216], which is contrary to the finding of hydride-induced transgranular-cracking across grains in Ti64 [31]. Adding to this, S. Cao et al. [213,214] found that absorbed H at the crack tip accelerated dislocation emission, enhanced the dislocation density, and introduced severe plastic deformation ahead of the crack tip that produced additional dislocations and eventually led to cracking. These studies make it apparent that SCC and HE at and ahead of a crack tip are highly dynamic processes and at very localized sites involving microstructure evolution, passive film formation/breakdown, chemical/electrochemical reactions, and dynamic environmental conditions.

Recently, S. Joseph et al. [217] suggested that a synergistic effect of O and H solute atoms in the solid solution is responsible for cracking in Ti-6Al-2Sn-4Zr-6Mo in an aqueous (D_2O) environment. This proposed scenario, in which O also plays a vital role, challenged the decades-old assumption that cracking of Ti alloys is related only to H (as interpreted by the HELP mechanism and the AIDE mechanism). This work inspires a new perspective for cracking studies that transition from a focus only on H towards the ingress of O—a critical insight for designing corrosion-resistant Ti-based materials.

It should also be noted that at this stage, none of the above mechanisms can be completely ruled out in favor of the others. Studies of the proposed mechanisms are at different stages of maturity and not always on the same materials or under the same conditions. As such, it is difficult to interpret characteristics beyond each individual experiment. Instead, it is necessary to carry out in-depth and highly systematic analysis to identify and validate missing characteristics, as well as to determine the conditions under which each of the representative mechanisms might manifest. Advances in both characterization capabilities and integrated multiphysics models could provide significant benefit for elucidating the different stages of cracking, including localized corrosion processes, crack nucleation, and crack propagation.

3. Opportunities and perspectives

Charting a course towards improving the performance of Ti metals and alloys in the presence of hydrogen relies on improved understanding of hydrogenation phenomena at the atomic to microstructural scales [34,35]. Achieving this understanding is an ongoing challenge, in large part because of the difficulty of making observations at the necessary length scales and deconvoluting causation associated with particular materials features. Integration of experimental approaches with modeling offers a unique opportunity to address these concerns [21,51–53,218–221]. Some general experiment-modeling integration strategies to probe relevant phenomena across multiple scales are presented in Fig. 2. Governing thermodynamic and kinetic processes associated with Ti hydriding are described in terms of composition and chemistry (atomistic scale), microstructure and mass transport (microstructural scale), and bulk hydriding and corrosion performance (macroscale). In each case, some physical quantities that can be both measured and modeled are identified, along with corresponding classes of techniques that can be utilized to achieve the handshaking between experiments and simulations: chemical spectroscopy, diffusion kinetics, phase growth/dissolution, and overall hydriding rate. The schematic in Fig. 2 underscores the need to combine multiscale models, multimodal materials characterization, and testing in order to achieve a holistic view

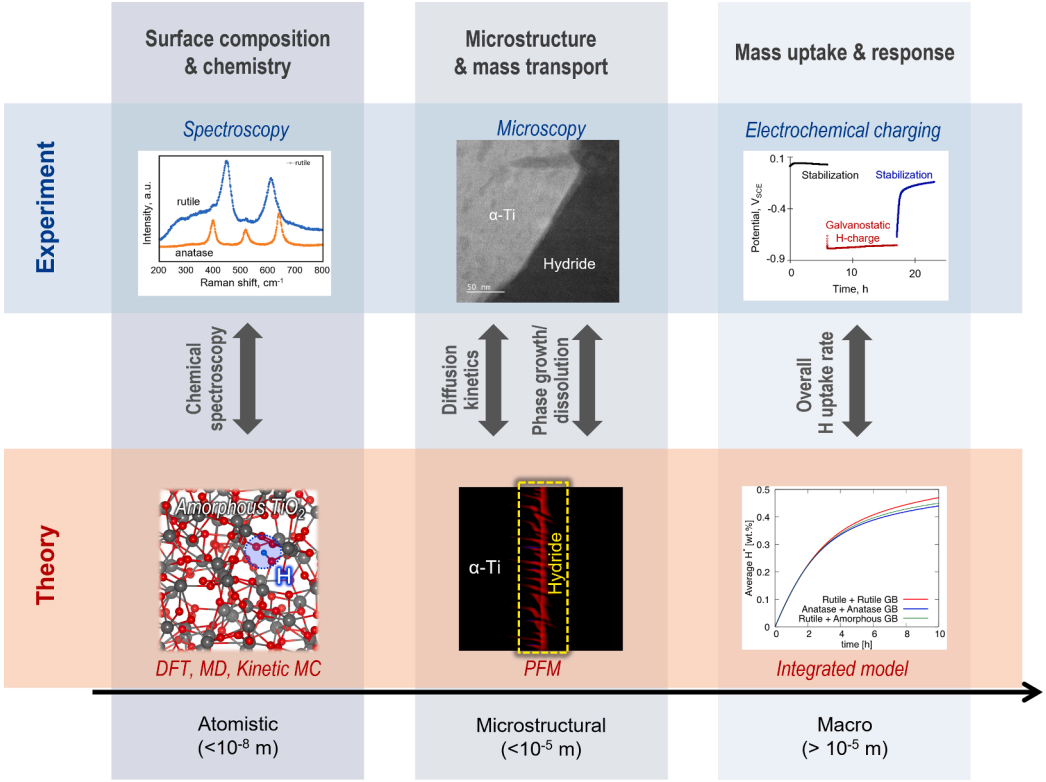

Fig. 2. Strategies for integration of advanced characterization and modeling to tackle challenges listed in Table 1 in Ti hydriding, with representative examples from the authors' work probing surface chemistry, mass transport, and hydrogen mass uptake. Top from left to right: Raman spectra for rutile and anatase TiO_2 native oxides at ambient conditions, dark field STEM imaging of hydrided α-Ti, and potential evolution during the galvanostatic H-charging on an α-Ti surface in deaerated NaCl solution. Bottom from left to right: DFT modeling of H atom in an amorphous TiO_2 native oxide, phase field modeling (PFM) of hydride formation in α-Ti, and integrated modeling of H uptake kinetics in TiO_2 native oxides with different phase and grain boundary composition approximations.

Table 5
Characterization methods, their capabilities, and the related challenges in Table 1 that can potentially be addressed using these methods. Shaded techniques (rows 2–6) are destructive, whereas unshaded techniques are non-destructive.

Methods	Length scale	Information	H/hydride associated defects	Associated challenges*
TEM-based (***ex/in situ***)	Sub-atomic to tens of μm	Atom position, lattice parameter, oxidation state, phase, microstructure, orientation, composition	Point defects, dislocations, boundaries, precipitates, nanocracks	1, 2, 3, 4, 5, 6, 7
SEM/EBSD-based (***ex/in situ***)	nm to mm	Phase, microstructure, orientation, composition	Dislocations, boundaries, microcracks, precipitates	2, 3, 4, 5, 6, 7
NanoSIMS (conventional/ flash-frozen)	50 nm to μm on lateral, nm in depth	H content, phase (qualitative), depth profile	Boundaries, microcracks, fracture surface, precipitates	1, 2, 3, 4, 5, 6, 7
APT (conventional/ flash-frozen)	Atomic to tens of nm	H content, composition (quantitative)	substitutional solutes, dislocations, boundaries, precipitates	1, 2, 3, 4, 5, 6, 7
TDS (***ex/in situ***)	Bulk measurement, ppm to sub-ppm	H content in bulk & defects, trap energies in defects (derived)	Point defects, dislocations, boundaries, precipitates	1, 2, 3, 5
SKPFM (***ex/in situ***)	nm to tens of μm	Topography, surface potential, H content	Boundaries, precipitates, microcracks	1, 2, 3, 5, 6, 7
ERAD	Tens of μm on lateral, nm in depth	H content (quantitative), depth profile	Charged surface	1, 4, 6
Neutron diffraction/scattering (***ex/in situ***)	mm spatial resolution	Atom position, lattice parameter, phase, orientation, strain	Point defects, Lattice displacement, precipitates, microcracks, charged bulk	1, 4, 5, 6
Neutron imaging (***ex/in situ***)	Tens of μm spatial resolution, 10 ppm mass resolution	H content (quantitative in 2D and 3D)	Precipitates, microcracks, macrocracks, charged bulk	1, 4, 5, 6
NRA	nm in depth	H content, depth profile	Charged surface	1, 4, 6
X-Ray diffraction/(imaging) (***ex/in situ/operando***)	Tens of nm to tens of μm on lateral, nm in depth	Lattice parameter, phase, strain, orientation, strain	Point defects, lattice displacement, precipitates, microcracks, charged surface	1, 2, 3, 5, 6, 7
XAS (***ex/in situ/operando***)	nm in depth	Local coordination, oxidation state, bond distances, phase	Electronic and point defects	1, 2, 3, 5, 6, 7

*Indicates the most closely relevant challenges that can be routinely studied but does not exclude the possibility of studying other challenges.

of Ti hydriding. Recent progress, opportunities, and perspectives in both experimental characterization and modeling will be discussed in this section, along with additional specific examples of proposed integration strategies.

3.1. Opportunities and perspectives in characterization methods

Although challenging, it is critical to develop and implement experimental characterization methods with high spatial resolution and dynamic capabilities. Table 5 summarizes the commonly used characterization methods, their capabilities, and the challenges listed in Table 1 that can be potentially addressed using these methods. For

example, leading methods for sample characterization include tomography and mass spectrometry for precise compositional analysis, and *in situ* or *operando* techniques like electron microscopy for structure and phase identification during the hydriding processes. Non-destructive, high-resolution experimental tools based on X-ray techniques and atomic force microscopy-based methods are likewise useful to collect information during materials degradation and have the advantage of doing so with minimal perturbation or impact of external factors, especially when these tools are employed *in operando* or *in situ* to monitor topography, phase, and electronic state evolution. In the case of hydriding, additional challenges arise from the difficulty of directly probing the tiny atom. Techniques based on neutron probes are particularly useful in this regard; additional hydrogen-sensitive characterization techniques are also documented in reference [222].

3.1.1. Development of high-resolution, localized hydrogen/hydride detection methods

3.1.1.1. Electron microscopy. Environmental electron microscopy, including environmental SEM and TEM [223,224], particularly when integrated with *in situ* nanomechanical testing, provides a powerful tool to investigate hydriding of metal alloys. The mechanical behavior of a hydrogenated matrix can be directly observed [197], and nanomechanical testing can be carried out on samples at the nano-to-micro meter scale e.g., nanopillars [225,226], nanowires [110], and nanocantilevers [107]. As an example of how this could be done, Xie et al. utilized quantitative environmental TEM nanomechanical testing [225] to report that dislocations in nanopillars of Al metal can be locked with hydrogen exposure and reactivated under cyclic loading without hydrogen exposure. Using a similar method, Yin et al. [110] observed that hydrogen suppresses the nucleation and movement of dislocations on the surface of Ag nanowires, rather than the usually reported hydrogen-enhanced dislocation nucleation and movement. Electron microscopy has also been applied to study hydriding of Ti-based metals. Q. Wang et al. [24] evaluated the orientation relationship between hydrides and the Ti metal matrix in CP titanium using an interrupted *in situ* electron backscatter diffraction (EBSD) setup. Kim et al. [30] developed an apparatus that combines electrochemical hydrogen charging in an aqeuous environment with a high vacuum-based SEM/EBSD capability to study the dynamic hydrogenation process of Ti64. The emerging electron channeling contrast imaging (ECCI) approach [227,228] has also shown to be very useful in revealing the correlation between subnanometer-scale H-dislocation interactions and micrometer-scale heterogeneous phenomena and mechanical response by imaging dislocations in larger-area grains.

However, it must be realized that it is challenging to directly observe hydrides based on contrast of collected images using electron microscopes; instead, indirect approaches are generally required. TEM usually needs to operate in electron diffraction mode to capture characteristic diffraction patterns specific to each type of hydride. SEM typically identifies hydrides through equipped EBSD by collecting phase maps or Kikuchi patterns and comparing them to known crystallographic phase databases. Interestingly, Kooi et al. [229] very recently demonstrated unprecedented imaging of H atoms and hydrides in Ti by developing an integrated differential phase contrast method in STEM mode. Some other limitations of electron methods include limited field of view and sample size, as well as reduced vacuum (gaseous environment) and occasional radiolysis of water (in humid or liquid cell environments), which can reduce resolution due surface contamination [223,224]. The sample preparation process for TEM (e.g., through electro-polishing or FIB) also tends to introduce H contamination and facilitates preliminary hydride formation if not controlled properly.

3.1.1.2. Secondary ion mass spectrometry (SIMS). SIMS techniques, including Time-of-flight (ToF) SIMS and NanoSIMS, have been used to analyze the surface and depth distribution of hydrogen, hydride, or hydroxide, and to correlate with microscopy (including 3D) of surfaces at microstructurally relevant length scales in Ti metals/alloys [17,27,29,133,220,230–240]. The advantages of SIMS are that it can analyze all elements (including H), distinguish isotopes, achieve extremely low detection thresholds (in ng/g or ppb range), and collect images of lateral chemical distributions (in certain instances) [236–239]. However, accurate SIMS analysis requires that the reference material be very similar to the studied material, given that sputter yields are highly dependent on chemical composition [239,241,242]. Therefore, SIMS is more often used for qualitative evaluation and visualization of hydrogen distribution and usually needs to be combined with other hydrogen-sensitive techniques for more reliable quantitative analysis. As an example, Y. Duan et al. [232] studied the influence of Ti-Mo interdiffusion on the distribution profile of deuterium (D) across TiDx/Mo films using the SIMS method, as well as a combined Rutherford backscattering (^{4}He$^-$RBS) and D(^{3}He,p)^{4}He nuclear reaction analysis (NRA) approach. It turned out that the SIMS-measured D concentration is remarkably smaller than the concentration obtained via RBS-NRA (this technique is discussed further below). Beam damage effects is another concern of SIMS, which compromises the analysis accuracy of localized hydrogen/deuterium signals [243].

3.1.1.3. Atom probe tomography (APT). APT utilizes a strong electric voltage to activate individual atoms of elements emitted from a needle-shaped sample, then chemically maps the 3D distribution of those elements [244]. APT is the only currently known technique with atomic spatial resolution that can precisely map hydrogen distribution and quantify its content in a material [33,34,161,165,166,217,245–247]. Independent researchers have further demonstrated that APT tips prepared by cryo-FIB can significantly lower hydrogen contamination compared with tips prepared under non-cryogenic conditions [34,166]. Cryogenic environment control throughout the sample tip preparation processes using, for example, cryo-FIB combined with a cryo-transferring chamber can further eliminate pre-existing H attached to samples [34,166]. These advances in technique development make it possible to properly leverage the unique advantages of APT towards analysis of hydrogen in Ti and Ti hydrides.

However, it is important to note that the APT tip can still be contaminated, usually in the range of 0.5–1.5 at%, by the residual H in the APT instrument chamber [35]. Hydrogen charging in a deuterium environment represents an alternative strategy that has been verified by others [165,166,246,247], although the noise from residual H in the collected spectra still perturbs the quantitative analysis to some degree. [165,166,246,247]. If other isotopes or used, it must be considered whether deuterium or tritium would exhibit the same segregation, phase, and distribution behavior compared to hydrogen, which is many cases is an unanswered question.

3.1.1.4. Flash freezing techniques. Beyond eliminating contaminations through cryo-environment control, an even more promising and exciting development involves the use of flash-freezing techniques, which have been successfully applied both to APT [248–252] and SIMS [253–255] at different length scales at solid–liquid interfaces. Flash freezing can "lock" the instantaneous elemental and ionic information (e.g., hydrogen, water, protons) at the regions of interest for performing "quasi *in situ*" analysis. For example, flash-frozen APT work [250] has been performed for 3D nanoscale analysis of composition and structure at the solid-water interface in corroded glass. These characterization advances should be transferable to hydriding studies of Ti, especially for trapping of H and local pH gradients in phase/grain boundaries, crevices, and matrix/inclusion interfaces. Depending on the size of the features of interest, APT, SIMS, or a combination of the two could then be adopted for analysis and data acquisition.

3.1.2. Development of non-destructive and in situ or operando methods

3.1.2.1. Scanning Kelvin probe force microscopy (SKPFM). SKPFM is a promising method to non-destructively detect H with high spatial resolution. It allows detection through a change in surface potential caused by H incorporation into the surface oxide and the matrix following hydrogen charging of the metal [42,256–263]. Direct quantification of H is made possible by applying a thin Pd layer, which effectively controls for the impact of oxide heterogeneity on hydrogen adsorption, thereby enabling the detection of limiting concentrations as low as 0.01 ppm and at nm resolution [40–46]. The measured surface potential via the Pd layer follows a logarithmic correlation with the charged H content [39,42]. It would be interesting to carry out feasibility studies of hydrogen adsorption quantification and hydriding phenomena in Ti alloys by coupling *in situ* SKPFM with an electrochemical charging process.

3.1.2.2. Elastic recoil detection analysis (ERDA). As a non-destructive and highly accurate quantification method, ERDA [264] can be used to measure both the lateral distribution at a resolution of tens of micrometers and the depth profile at a resolution of nanometers for light elements such as H and C. A beam of projectile ions that are usually heavier than the light elements to be probed collides elastically with the nuclei of the light element targets, ejecting them from the matrix material. ERDA has been successfully used to study H distribution in Ti64 by measuring the volume density [265] and depth profile [151,266]. Note that despite its usefulness in depth profiling, ERDA has relatively low lateral resolution and accumulative signals. As such, it should be classified as a surface-averaged measurement tool.

3.1.2.3. Thermal desorption spectroscopy (TDS). TDS is a reliable tool to collect information pertaining to H trapped in metals and alloys. The lattice H concentration, the reversibly incorporated H concentration and the irreversibly trapped H can all be estimated through desorption spectra. TDS also enables analysis of trapped energies at different types of matrix defects (e.g., vacancies, interstitial sites, dislocations, precipitates, and grain boundaries) [90]. Note that the accuracy of such analysis is typically around 0.1 eV for the binding energy. Uncertainties can be ascribed to surface defects, inaccuracies of temperature monitoring devices, and microstructure thermal instability. In interpreting TDS data in terms of H binding energies, one must remember that the temperature of H release implicitly contains information regarding both thermodynamic and kinetic factors, which can be difficult to disentangle if significant kinetic limitations are active.

3.1.2.4. Neutron diffraction and imaging. Hydrogen adsorption, transport and hydriding phenomena in the bulk materials can be studied non-destructively via neutron-based techniques such as neutron diffraction, scattering, vibrational spectroscopy, and imaging. For example, *in situ* neutron diffraction was utilized to study the decomposition of Ti hydride powder during constant heating in Ar environment [267]. *In situ* and *operando* neutron imaging was used to investigate the structural stability and the spatiotemporal H distribution in bulk (up to 40 mm in diameter) metal hydride composites (hydrided Hydralloy) [268]. In a similar vein, SCC phenomena associated with low H content (10 – 300 ppm) in Zr alloys were studied using neutron imaging with a mass resolution of ~ 5 wt ppm and a spatial resolution of ~ 25 μm [269].

3.1.2.5. X-ray techniques. XRD as a non-destructive and readily accessible method that is particularly useful for studying surface/sub-surface hydriding phenomena relating to hydride nucleation, lattice degradation, phase transformation, and cracking or fatigue. In addition to bulk phase identification, strain effects correlating to H content can be probed. For example, the evolution of the lattice parameter of δ-TiH_x, which depends on the H concentration in pure Ti samples, was determined by XRD measurements in the Bragg-Brentano symmetric geometry using Co K_α radiation [19]. Liu et al. used the technique to estimate different hydride compositions, identifying a primary composition of $TiH_{1.5}$ (δ hydride), with a small fraction of $TiH_{1.7}$ and TiH_2, in electrochemically charged pure Ti [17].

In situ or *operando* XRD has also been shown to be very powerful to collect the dynamic information of hydriding phenomena in Ti, Zr, and Pd [128,185,186,211,221,270–274].[128,185,186,211,221,270–274]. In particular, 3D X-ray diffractive imaging (XRDI) is a new *in situ*/operando X-ray imaging technique developed to resolve 3D distributions of strain and phase transformations of solid materials exposed to reactive environments [36,275–277]. For example, Ulvestad et al. [118] used 3D XRDI to monitor the strain and phase transformation evolution during hydriding of Pd nanocubes and corroborate strain distributions with H concentration distributions. Hahn et al. [221] revealed the dynamics and hysteresis mechanism of H-Pd interactions during intercalation and deintercalation based on a multimodal *in situ* XRD and absorption spectroscopy (XAS) apparatus.

XAS has also been demonstrated as a probe of phase composition within Ti hydrides [278]. Although less direct than XRD for phase identification, XAS has the intrinsic advantages of sensitivity to both surface and bulk regions depending on the collection mode (electron and fluorescence yield, respectively), as well as the ability to probe hydrogen effects on electronic structure in non-crystalline local environments or prior to hydride phase formation. The combination of X-ray-based multimodal diffraction, spectroscopy, and microscopy could open a new characterization frontier to understand various metal hydriding phenomena.

3.1.2.6. Nuclear reaction analysis (NRA). Through the resonant reaction $H(^{15}N, \alpha\gamma)^{12}C$ [279] or non-resonant reaction $D(^3He,p)^4He$ [232], nuclear reaction analysis (NRA) is capable of quantitatively depth profiling and non-destructively measuring H (or D) content distribution at solid surfaces, subsurfaces, and interfaces. The method utilizes a ^{15}N or ^3He ion beam to detect the H or D isotope in a depth range of up to 1–2 μm. The near-surface depth resolution is a few nanometers for surface-normal ion incidence and can be further improved to 1 nm by applying a grazing-angle beam. NRA can measure hydrogen with a surface concentration of ~ 10^{13} cm^{-2} (~1% of a typical atomic monolayer density) and volume concentration at a sensitivity of ~ 10^{18} cm^{-3} (~100 at. ppm). NRA has been successfully demonstrated in some hydriding studies including: quantitative measurement of surface and bulk H concentration in the near-surface region of a H-treated Pd single crystal [280]; determination of H depth and density near the interfaces of thin SiO_2 films and Si(1 0 0) substrates [280]; and depth profiling of D, Ti, and Mo in metal hydride films (TiD_x/Mo) [232].

3.2. Opportunities and perspectives in multiscale modeling

In close concert with experimental probes, multiscale, multiphysics models have a key role to play in providing foundational understanding of Ti hydriding. Here we focus on predictive models that range from atomistic to mesoscopic to macroscopic, which are emerging as a powerful tool for generating “synthetic data” that can be treated on equal footing with measurements for unbiased comparison. Table 6 lists several classes of methods that can provide much-needed insight, whereas Fig. 2 shows how these models can provide tie-ins with experiments (Table 5) to more comprehensively address the challenges listed in Table 1.

In general, the methods fall into two categories: atomistic/discrete methods and continuum methods. The first category includes first-principles and quantum chemical approaches (most notably, DFT), as well as DFT-based molecular dynamics, which provide high-accuracy energies, forces, charge states, and atomic positions, as well as thermodynamics for phase diagram prediction, but are limited to very small

Table 6
Modeling methods at multiple scales, their capabilities, and the related challenges in Table 1 that can potentially be addressed. Shaded techniques (rows 2–4) are atomistic or discrete, whereas unshaded techniques are based on continuum approaches.

Methods	Length/time scale	Information	H/hydride associated defects	Associated challenges*
DFT- and quantum chemistry-based	Atomic to tens of nm	Bulk and surface energies, absorption site energies, lattice parameters, migration barriers, oxidation/charge states, relaxed atomic positions, phase diagrams	Point defects	1,2,3,4,5
Molecular dynamics (DFT-based and force-field)	Atomic to tens of nm for up to 100 ps (DFT-based); Atomic to μm for up to 100 ns (force-field)	Diffusion, segregation, trapping	Point defects, dislocations, grain/phase boundaries	1,2,3,4,5,7
Coarse-grained atomistic (KMC, coarse-grained MD)	nm to μm for up to μs or ms	Diffusion, segregation, trapping	Point defects, dislocations, grain/phase boundaries, nucleation	1,2,3,5,7
Phase-field modeling	Tens of nm to mm for up to tens of ms	Hydride phase nucleation-and-growth, composition, microstructure-aware diffusion, stress distribution	Grain/phase boundaries, microcracks, precipitates, inclusions	1,2,3,6
Finite element modeling	μm to cm for up to seconds	Stress distribution, transport, cracking	Microcracks, precipitates	6
Integrated kinetic modeling	Macroscale	H uptake rate	None (can be incorporated through effective parameters)	3

*Indicates the most closely relevant challenges that can be routinely studied but does not exclude the possibility of studying other challenges.

or ideal systems for short times. Other atomistic methods include force-field based molecular dynamics (MD) for simulating local diffusion, segregation, and trapping, in addition to coarse-grained approaches such as kinetic Monte Carlo (KMC) for transcending much larger ranges of time scales. On the continuum side, more complex models that incorporate microstructural features and nonequilibrium conditions can be incorporated, but at the expense of physical accuracy. Among the continuum methods, phase-field modeling (PFM) provides a highly flexible framework for analyzing phase transformation, microstructure evolution, and chemomechanical coupling under different environments. This approach can be well integrated with atomistically derived quantities, as detailed in the sections below. Finite-element models (FEM) lack the flexibility, resolution, and microstructure awareness of the phase-field approach, but are well suited to examine solid mechanics and fracture effects. Finally, integrated kinetic models can be built around parameterized nucleation-growth and diffusion equations to simulate the full hydriding process; unfortunately, these models typically forego details of microstructure and defect interactions and are therefore less useful for addressing the gaps in Table 1. In addition, they are typically empirically fitted and therefore provide minimal predictive capability beyond the specific conditions and materials for which they were parameterized. Nevertheless, we include them here because they can retain some predictive power when coupled with finer-scale modeling approaches to obtain needed parameters. The following sections detail three key needs for progressing modeling methods to better address hydriding issues in Ti and other metals: multiphysics integration, multiscale integration, and incorporation of beyond-ideal factors.

3.2.1. *Multiphysics integration*

One of the major challenges in modeling metal hydride formation and associated microstructures is the involvement of concurrent chemical, physical, and materials processes, as well as their complicated (and often unknown) coupling. For instance, to comprehensively account for nucleation and growth of hydride phases in realistic polycrystalline Ti and its alloys, the model should incorporate surface reactions; surface, grain, and boundary diffusion, thermal transport, grain boundary H segregation, crystallographic structural transformations, and mechanical interactions involving large volume changes. Of the available approaches, perhaps the most versatile in this regard is the phase-field method [281–283], which has provided a general framework for integrating these multiphysics phenomena for modeling phase transformations and associated microstructure evolution in a wide variety of structural applications [284], energy applications [285], and functional applications [286]. PFM is based on a diffuse-interface description and can track the evolution of a diffuse grain, phase, or particle boundary according to underlying governing physical equations. As such, it can easily be extended to include different physicochemical phenomena, provided the necessary parameters and functional relationships can be properly defined.

For modeling hydride formation in metals using PFM, α -Zr (hcp) has often been employed as a model system [287,288]. The fundamental

physical processes, including hydrogen diffusion, crystallographic structural changes, and elastic interactions, were first integrated in the context of the diffuse-interface description to model the coherent nucleation and growth of the γ Zr hydride by Ma et al.[289]. This phase-field model was subsequently extended to account for the effect of an applied load [289], grain boundaries [290], and the non-uniform stress field near a blunt notch [291]. Guo et al. incorporated elastoplastic effects involving large volume expansion into the phase-field modeling framework [292], which was applied to simulating γ hydride formation near structural flaws, including cracks [293]. Similar models were developed and applied to analyze metastable hydride phase formation involving inhomogeneous elasticity [294,295] and its role in nucleation-and-growth mechanisms of the stable δ Zr hydride phase [296]. More quantitative phase-field models that account for temperature-dependent thermodynamics and materials parameters have also been discussed [297,298]. Han et al. employed the micromechanical phase-field model to investigate more detailed microscopic features of the δ Zr hydride microstructure, focusing on stacking of microplates and their reorientation behavior [299].

Recently, Heo et al. established a comprehensive phase-field model for simulating hydride formation with general metal/hydride interfacial coherency in a generic polycrystalline Zr system [50]. Because hydride formation in α -Ti exhibits very similar features and characteristics to Zr, this same framework can directly be applied to model Ti hydride formation. Preliminary simulations along these lines are reported in Section 3.3, wherein we have parameterized the model to simulate reaction-induced hydride formation in polycrystalline pure α -Ti using available materials databases (e.g., thermodynamic free energies [300], diffusivities [89,301], elastic modulus (in Table 4), etc.). A more detailed description of this work is forthcoming.

Despite the power of PFM and related continuum approaches to integrate multiphysics factors within a single framework, the underlying governing relationships must be known or readily derivable. Because defects, compositional heterogeneity, microstructure, and other factors discussed in Section 2 play an important role in determining local interaction with H, determining such relationships in practice can be extraordinarily difficult. Moreover, if nonequilibrium hydriding kinetics are to be properly incorporated, then the effects of the environment must likewise be considered either implicitly or explicitly. In our view, this is best accomplished by incorporating a combination of experimental inputs and atomistic modeling inputs to extract important parameters and functional relationships. Examples of needed quantities for accurate PFM include phase free energies, detailed microstructures, diffusivities, interfacial and surface energies, and elastic constants.

3.2.2. Scale integration

Another challenge closely related to the need for multiphysics model integration is the intrinsically multiscale nature of hydrogen-material interactions. In general, each of the methods listed in Table 6 can be integrated with other modeling methods to extend scales of space, time, or both. For example, KMC methods are well suited to extend atomistic simulation times to experimentally relevant scales by incorporating DFT- or MD-derived kinetic barriers, provided events can be discretized (e.g., diffusion or trapping) and mapped onto a regular lattice. However, it is far more challenging—yet ultimately more impactful—to integrate discrete atomistic approaches and continuum approaches. This combination can leverage the superior accuracy and capability of atomsitic approaches to account for local features such as point defects, while also appealing to the microstructure awareness and rapid nonequilibrium simulation capabilities inherent to many of the continuum approaches.

Along these lines, H-dislocation interactions and hydriding phenomena were recently explored via multiscale approaches in which thermodynamic and analytical models were combined to achieve both atomic-level resolution and continuum-level computational efficiency [48,49,108]. These approaches allow for determination of the concentration of hydrogen at the atomic scale upon perturbation of thermodyamic variables, including temperature and hydrogen chemical potential. In general, the thermodynamic parameters are linked to, and controlled by, continuum-scale models (e.g., FEM or PFM).

Another example is the integrated thermodynamic and analytical model developed by Leyson et al. [49]. In this model, input parameters (e.g., H-H interaction energies) were derived from coupled embedded atom force-field and Monte Carlo simulations. The integrated model assessed the dependence of hydride size on environmental temperature and bulk hydrogen concentration and also successfully predicted both nanometer-scale hydride nucleation and the activation of hydrogen-enhanced local plasticity. A sharp transition from a non-hydride-forming domain to a hydride-forming domain was identified, for which the transition point was characterized by a critical hydrogen chemical potential for hydride nucleation. The predicted results were also consistent with nanoindentation tests carried out on H-charged materials.

Similarly, Zhao et al. [108] developed a continuum model, the so-called hydrogen-informed expanding cavity model, that was calibrated by the large-scale MD simulations. This model incorporates the collective interactions between hydrogen and dislocations and their impact on softening of HE metals and alloys. The simulation results show that the activation energy for dislocation nucleation decreases with the concentrated local H, leading to decrease in indentation force and hardness. Note that this behavior is consistent with the hydrogen-promoted dislocation migration and multiplication along with the matrix softening reported by many studies as discussed above.

The PFM examples discussed in the previous section provide additional opportunities to improve multiscale integration. DFT, MD, and KMC simulations can provide transport data, whereas DFT and force-field models can provide needed interfacial energy and solid mechanics inputs. Some specific examples of how this can be done are provided in Section 3; nevertheless, additional progress is needed to incorporate the needed diversity and complexity into the lower-length scale simulations. A particular priority involves modeling static and dynamic properties of disordered and heterogeneous systems including grain and phase boundaries, as well as amorphous surface oxides that offer unique configurational and chemical challenges at the interface with the Ti metal.

3.2.3. Beyond ideal models

To correctly capture physical, chemical, and materials behavior in simulations of hydriding phenomena, it is important to incorporate models capable of transcending idealized crystalline structures and purely thermodynamic considerations. Critical frontiers in computation include the development of models with more sophisticated and coupled physics, more realistic microstructures, more complex atomic configurations of interfaces and boundary regions, and better approximations of real operating conditions.

This need was recognized in a recent paper outlining how “beyond-ideal” factors could be incorporated at both the atomistic and continuum scales to improve hydriding models being developed by within the Hydrogen Materials—Advanced Research Consortium (HyMARC) [51]. In that study, four key beyond-ideal factors were identified and shown to influence performance predictions in hydriding reactions: (1) surface anharmonic dynamics; (2) interface and surface energy penalties; (3) mechanical stresses induced by constrained volume expansion; and (4) the presence of the native surface oxide. Although the focus did not include Ti, the identified beyond-ideal factors echo many of the themes introduced in Table 1 and Section 2. An additional priority is the development and application of methods capable of evaluating the

properties of Ti surface oxides, which are notoriously configurationally complex. Graph neural network-based approaches [302] are emerging as a promising approach to quantify and efficiently explore this complexity and are currently being applied by our team to investigate H in TiO_2 films.

Another challenge involves accounting for atomistic defect interactions within continuum models that are otherwise incapable of achieving the necessary fidelity. One example of such an approach that has achieved widespread use is the point defect model (PDM). The PDM has been applied to predict the growth or dissolution of oxides and hydrides in hydride-forming metals, typically by integrating experiments and numerical models [52,53]. For instance, Ai et.al. [52,53] employed the PDM to analyze H-associated degradation mechanisms in pure Zr in hydrogenated pressurized water reactor primary coolants.

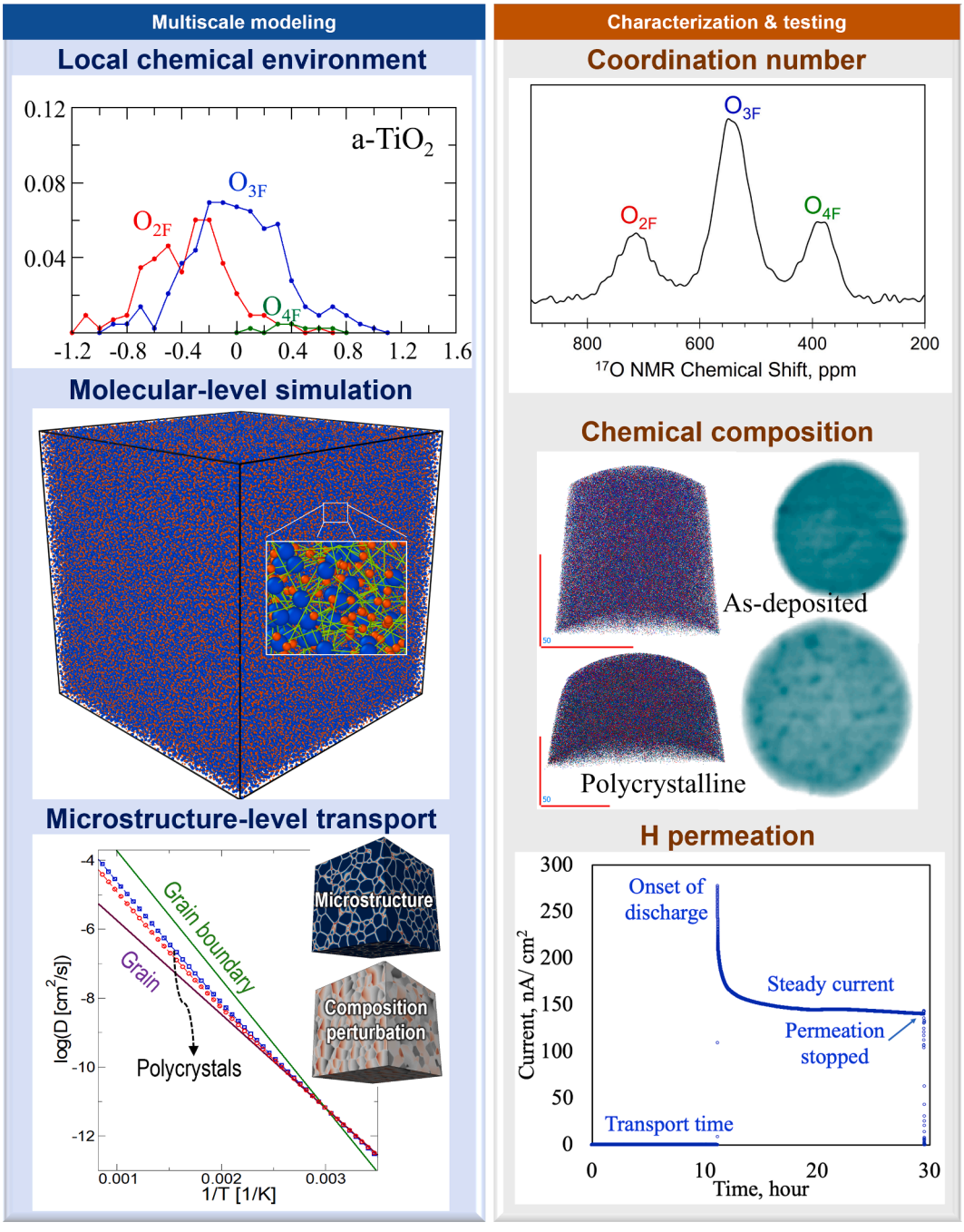

Fig. 3. Modeling and experimental integration strategies for studying hydrogen transport and trapping in surface Ti oxides, with specific examples from the authors' work. Computational approaches on left side, top to bottom: Relative probability of H binding energy (in eV with respect to H_2) at diverse local sites in amorphous TiO_2 (α-TiO_2) with respect to oxygen coordination number (2-fold [2F], 3-fold [3F], 4-fold [4F]); KMC setup for molecular modeling of H hopping in a-TiO_2 based on a graph neural network description (inset shows Ti (blue), O (red), and Ti-O bonds (green) within the network); mesoscopic continuum modeling of hydrogen diffusion through a complex microstructure in polycrystalline TiO_2 (insets: input microstructure and corresponding prediction of local variation in H composition). Experimental approaches in right side, top to bottom: NMR measurement of O coordination number distribution in ^{17}O-labeled a-TiO_2, APT analysis of as-deposited (top level) and polycrystalline (bottom level) Ti oxide film showing compositional variations (scale bar: 50 nm) indicative of interfaces and local heterogeneities; measured H permeation through a 400 nm thick as-deposited Ti oxide film on Ti metal using a Devanathan cell as a function of charging time in an aqueous environment (charging current: 200nA/cm^2, discharge potential: 0.2 V_{SCE}, electrolyte: deaerated 0.6 M NaCl).

They found that the barrier layer comprises hydrogen-deficient zirconium hydride (ZrH_{2-x}), while the outer layer comprises porous, stoichiometric ZrO_2 that forms via hydrolysis of ZrH_{2-x} at the interface between the layers. This analysis indicates that corrosion resistance depends on the physical features of the porous oxide layer, including its porosity and thickness. Furthermore, hydride platelets were found to precipitate below the metal/barrier layer interface, with their number density decreasing with distance from that interface [53]. This behavior verifies that hydride platelets form due to atomic H that diffuses through the metal phase from the interface with the barrier layer. Importantly, this mechanistic understanding provides practical guidance on slowing hydriding by engineering the porosity and/or thickness of the outer layer for enhanced outer-layer resistance.

Considering the mechanistic similarity between Ti hydriding and Zr hydriding, the PDM could likewise be applied to predict key aspects of hydriding and hydrogen-induced corrosion of Ti and its alloys. For electrochemical charging, the PDM could be optimized to describe the partial anodic process and incorporate cathodic hydrogen evolution. The optimized model could then be used to compute the passive dissolution rate, allowing for reliable estimation of the time to perforation of the porous oxides layer. Once perforated, hydriding of the base Ti alloy would occur. The thickness of the barrier layer becomes larger as the potential is made more negative and can serve as a reliable measure of the extent of hydriding, which can in turn be predicted by the PDM based on *in situ* EIS measurements along with optimized model parameters [52,303]. Suggested details of how PDM could be applied to studying Ti hydride growth process are provided step-by-step in the supplementary information.

3.3. Examples of experiment-model integration

In this section, we provide representative examples of our current efforts to more closely integrate experiments and models to investigate some of the key thermodynamic and kinetic mechanisms associated with Ti hydriding. These examples, which are outlined alongside preliminary representative results in the subsequent sections, demonstrate the feasibility of the integrated approach for analyzing coupled chemical, physical, and materials processes that constitute hydrogenation of Ti. In particular, we focus on probes of three key governing phenomena: (1) H transport through the protective Ti surface oxide; (2) micromechanical response of surface oxide to hydrogenation of underlying Ti; and (3) the beginnings of hydride formation in polycrystalline Ti.

3.3.1. H transport through Ti surface oxide

Fig. 3 illustrates how experiments and models can be integrated to probe the effects of local binding characteristics and microstructural features on hydrogen transport in stoichiometric and nonstoichiometric titanium surface oxides (TiO_x) at multiple length scales. As discussed in Section 2.1, this oxide layer forms at the Ti metal surface in service, and understanding its interaction with H is critical for elucidating the key processes in early-stage hydrogenation of Ti and its alloys. The TiO_x oxide layer incorporates a variety of chemical and structural complexities, including atomic structural disorder, non-stoichiometry, and structural defects such as grain boundaries.

To isolate physicochemical factors that determine the impacts of the structural complexities on hydrogen transport at the atomic level, quantum–mechanical computational approaches based on DFT can be employed. Such approaches are uniquely capable of interrogating the relationship between relevant local atomic structures of the oxide and the associated H binding characteristics. Ab initio molecular dynamics simulations can be used to generate both ordered and highly disordered atomic structures of TiO_x, which can then be analyzed to identify classes of unique environments for hydrogen binding, parameterized by structural factors such as the local oxygen coordination number (Fig. 3, top left). Particularly for atomically disordered regions, it is critical to validate that the models are correctly capturing the available local environments. For this purpose, we can use DFT to compute spectral "fingerprints", which can be compared directly to measurements. One example of is NMR, which can probe the relative expression of local O coordination environments throughout the sample (Fig. 3, top right). In addition to validating the possible local environments in the oxide, such spectroscopic measurements can be used to "tune" the model towards a calibrated result that better expresses the correct fraction of local environments found in the material.

Having validated the unique local environments, we can proceed to compute hydrogen hopping events among them. Coarse-grained featurization using graph neural network-based approaches aid in rapidly analyzing the role of diffusion network topology within the complex oxide (Fig. 3, center left). This analysis informs kinetic Monte Carlo simulations, by which hydrogen hopping kinetics in TiO_x is directly extracted. The network models can be informed and validated by precise elemental distribution and composition analysis of TiO_x using APT, which provides a compositional and microstructural guide to inform factors such as stoichiometry (Fig. 3, center right).

Finally, the measured microstructural features are reproduced in digital representations using PFM, and the microstructure-level effective diffusivity of hydrogen through TiO_x is computed in the presence of different microstructural features (e.g., grain size, grain boundaries, crystallinity fraction, and compositional variation). This can be done using a microstructure-aware mass transport modeling approach, such as the one our team recently reported for complex oxides [304] (Fig. 3, bottom left). This mesoscopic modeling approach incorporates input diffusion parameters from atomistic simulations and digital representations of realistic oxide microstructures. Fig. 3 (bottom left) shows an example of computed effectivity diffusivities of hydrogen in polycrystalline TiO_x (see figure inset for the corresponding input microstructure) at different temperatures. The resulting H transport prediction can then be compared to independent measurements of H permeation. At mesoscopic (e.g., grains) and macroscopic (e.g., entire film) levels, hydrogen diffusion through Ti oxide thin film can be evaluated experimentally by gaseous permeation or electrochemical permeation. Fig. 3 (bottom right) includes an example of electrochemical permeation of hydrogen under controlled environment through a Ti oxide thin film. The onset of discharge on the anodic side of the cell indicates the permeation of hydrogen through the film and metal foil. Diffusion coefficients can be estimated from such measurements and compared with mesoscopic effective diffusivity calculations with identical microstructural features and chemical composition (We caution that microcracks in the oxide films can affect these measurements; however, such effects can be partially compensated by comparing charging and discharging currents.). Having validated the model, we can then proceed to systematically quantify the impacts of microstructural features such as grain size, grain morphology, and grain boundary types on hydrogen diffusion properties in TiO_x.

3.3.2. Micromechanical response to H incorporation

Fig. 4 shows how the relationship between microstructure and mechanical response of the surface oxide to hydrogenation-induced strain can be assessed by combining experiments and simulations. As discussed in Section 2.3, hydrogenation of Ti metal involves significant volume expansion, which exerts mechanical strain within the oxide layer on the metal surface. The associated lattice distortion in the oxide can affect hydrogen transport kinetics or cause physical damage (e.g., cracking) to the surface oxide layer, potentially accelerating hydrogen permeation through the layer [305]. When analyzing the mechanical response of the oxide layer, additional potential complexity may arise from possible phase transformations or hydrogen reactions activated by the exerted strain [305].

The relevant phase and reaction behavior in TiO_2, as well as their sensitivity to microstructural features, can be probed experimentally via controlled experiments employing TiO_2 thin films with varied microstructures. Fig. 4 (top left) shows examples of crystalline TiO_2 surface

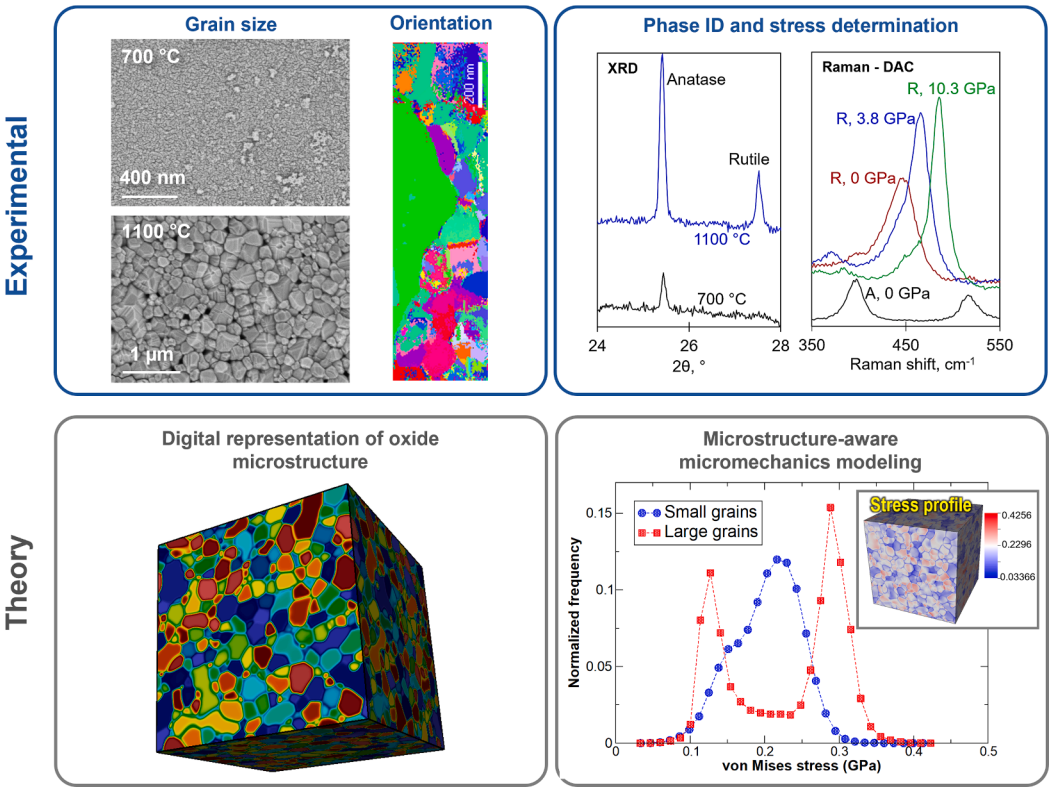

Fig. 4. Modeling and experimental integration strategies for probing micromechanical response to H-charging in Ti oxide thin films, with specific examples from the authors' work. Experiments provide microstructure inputs for modeling, which facilitates comparison between predicted stress distributions and the measured phase mechanical response. Experiments in top row (left to right): Ti oxide thin film with different grain sizes (SEM images) and orientations (EBSD image) obtained by deposition and subsequent thermal treatment; XRD and *in situ* DAC-Raman spectra (in an H_2 environment). Simulations in bottom row (left to right): digital representation of an Ti oxide microstructure simulated using PFM; predicted distribution of local Von Mises stresses for two different Ti oxide grain sizes based on mesoscopic microstructure-aware micromechanics modeling.

films produced with grain sizes ranging from ~ 5 nm to ~ 200 nm by ion beam sputter deposition method and subsequent thermal treatment. Electron microscopy is used to determine grain structure, whereas XRD is used to identify phases. Fig. 4 (top right) demonstrates that the anatase phase is the only crystalline phase during thermal treatment at an intermediate temperature (700 °C), whereas both the anatase and rutile phases are present at 1100 °C. The impact of mechanical loading on the phase and hydrogen reaction behavior is gauged by monitoring phase evolution and strain of TiO_2 *in situ* under pressure loading in an H_2 environment in a diamond anvil cell (DAC) coupled with Raman

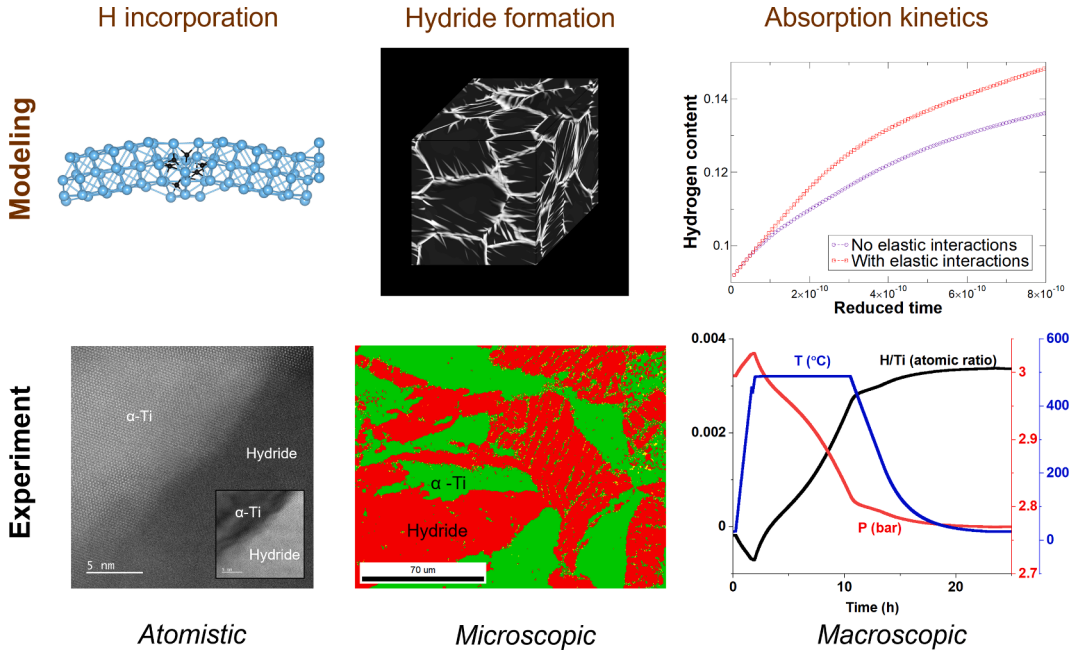

Fig. 5. Modeling and experimental integration strategies for investigating hydride phase evolution in Ti metal and its correlation to H absorption across atomistic, microscopic, and macroscopic scales. Modeling in top row (left to right): DFT-MD simulation of H incorporation within a model grain boundary of Ti as inputs for PFM; PFM of hydride formation; and results from PFM-based integrated modeling of hydrogen uptake kinetics. Experiments in bottom row (left to right): dark field STEM imaging (inset: bright field) of α-Ti/hydride at lattice resolution; EBSD phase maps of Ti hydride phase distribution in α-Ti metal; and macroscale H-charging/absorption kinetics of a Ti disc (2 mm in thickness and 8.5 mm in diameter) with respect to time, temperature, and pressure.

spectroscopy. In this case, the strain is visible, although no evidence of hydriding is detected in the Raman spectroscopy measurement up to 30 GPa at ambient temperature.

A companion computational effort involves the design of a microstructure-aware micromechanics modeling approach [306] to analyze the mechanical response of polycrystalline TiO_2 to the tensile strain caused by the volume expansion associated with hydriding of the underlying Ti metal. First, a microstructural representation is produced (Fig. 4, bottom left) using PFM or direct tomographic reconstruction to match the experimental grain structure. Next, the stress distribution within this digital microstructure is computed based on local elastic moduli of the individual grains, as parameterized from DFT calculations. Fig. 4 (bottom right) shows how von Mises stress distributions qualitatively differ for two average grain sizes. Based on these computed distributions, we can identify mechanical "hotspots" featuring extreme local stresses that might initiate cracks or induce phase transformations. By further combining with experimental mechanical testing and microstructural probes, the models can in principle be calibrated to quantify the relationship between oxide microstructural features and observed micromechanical and phase behavior.

Note that by combining models with experiments, we can directly probe local stress variation within the oxide film under hydriding conditions, as well as isolate the micromechanical effects within the film from those of the underlying metal substrate. By comparison, direct measurement of stress distributions within an isolated, standalone thin oxide film without a supportive substrate would be extremely challenging experimentally. As an alternative, TiO_2 thin films could instead be deposited onto a carefully selected substrate, or else well-controlled bulk TiO_2 could be used. The latter solution would also enable use of bulk experimental probes such as XRD, permitting monitoring of average lattice deformation and strain accumulation during hydrogen charging and transport for direct comparisons with model predictions as a function of microstructure.

3.3.3. Hydride phase formation

Fig. 5 shows how hydride phase formation at grain boundaries and related microstructural features within Ti metal can be probed at three different scales by combining simulations and experiments. Here, experimental and modeling approaches are synergistically combined to examine multiscale mechanisms incorporating coupled physicochemical processes and metal microstrucutral effects that determine the hydrogenation kinetics and the associated hydride phase microstructure evolution. Experimental and modeling efforts benefit one another by providing input parameters, measurement or simulation conditions, and cross-validation.

The modeling effort begins with atomistic DFT and MD simulations of grain boundary structures to compute hydrogen incorporation and segregation energetics (Fig. 5, upper left). The simulations are performed in concert with experimental characterization of α-Ti/hydride interfaces and grain structures using electron microscopy at lattice resolution (Fig. 5, lower left).

Next, we adapt a mesoscopic PFM approach to simulate hydride formation and corresponding microstructure using the model formulation by Heo et al. [50] (Fig. 5, top middle). The PFM simulations account for multiple multiphysics factors governing hydriding of polycrystalline Ti. including the thermodynamic driving force [300], hydrogen diffusion rates [301], crystallographic structural changes [283], micromechanical interactions [282], hydrogen-grain boundary/surface interactions [307,308], and hydrogen reactions at the surface. The atomistic simulations provide key parameter inputs for these quantities. To analyze and quantify the realistic metal microstructural impacts on the hydride formation tendency and kinetics, it is further necessary to include experimentally relevant microstructural features and reliable energetics related to experimentally probable grain boundaries. As such, we also analyze the spatial distribution of hydrogen (H or D) and hydride in Ti microstructures based on imaging data (Fig. 5, bottom middle), which are then compared with simulated hydride phase microstructures. For instance, the orientation relationship between the growing hydride phase and the α-Ti metal phase can be captured using EBSD, providing information comparable to PFM-modeled α-Ti/hydride mixed microstructures.

Finally, a fully integrated model based on PFM allows us to simulate the overall H absorption kinetics within the metal microstructure under controlled conditions (Fig. 5, top right). The validity of this integrated model is verified by comparing the PFM results with experimental measurements performed at the macroscale (Fig. 5, bottom right). For instance, the experimental hydrogen uptake curves as a function of H-charging time and/or temperature under controlled hydrogen pressure can be collected via a pressure-composition-temperature (PCT) apparatus. The model-predicted and PCT-measured hydrogen uptake behavior represent macroscopic characteristics of hydriding resulting from collective effects of the involved multiphysics factors, allowing for direct comparison. The model can then be used to probe various "what if" scenarios in which materials or environmental parameters are altered. Various physical ingredients can also be turned off to explicitly isolate their effects, as in the example of elastic micromechanical interactions given in Fig. 5 (top right). In addition, by linking performance to H-metal interactions across all three scales (atomistic, microscopic, and macroscopic), we can in principle distinguish reversible (e.g., H in hydride phases) and irreversible (e.g., H in trapping sites) H contents, with implications for developing practical microstructural or compositional engineering guidelines for improving performance or degradation resistance.

3.4. Summary

Recent advances in multiscale, multiphysics simulation and modeling, as well as ongoing improvements in the resolution and sophistication of experimental probes, continue to provide new opportunities to address lingering unknowns in Ti hydriding. However, in our view, it is the integration of atomistic and continuum simulations with multimodal experimental characterization that offers the highest value. Indeed, such integration has already begun to elucidate contributing factors in several key underlying phenomena. The demonstrated examples for hydrogen transport in surface oxide, micromechanical responses of surface oxide, and hydride formation in polycrystalline Ti illustrate how improved experiment–theory integration might be achieved. Nevertheless, these examples represent only a few of the many emerging integrated approaches for examining atomistic and microstructural impacts that could be applied in the near future to understand thermodynamics and kinetics of Ti hydriding. Additional extensions should be prioritized to account for more complex hydrogen-related phenomena, including hydriding-induced cracking and hydrogen-dislocation interactions, which form key bases for analyzing mechanical failure mechanisms due to hydrogen exposure.

Opportunities are also available for improvements in the models to better facilitate direct comparisons with experiments. For instance, as first-principles simulations of complex surfaces become more routine, the feedback cycle between spectroscopic predictions and measurements can be expected to play a much larger role in elucidating the effects of surface chemistry and other materials features on hydriding. By using model systems that represent features of realistic systems under working conditions, first-principles methods can also be employed to illustrate the specific relationship between surface chemistry and transport at the interface, and to identify the most impactful materials or environmental factors. Likewise, mesoscopic "microstructure-aware" models can be used to integrate atomistically derived parameters with inhomogeneous microstructural features that match experimental realities, allowing far more representative investigations of hydrogen-materials interactions under more realistic conditions. Capturing such nuances is likely to prove increasingly important as our understanding of Ti hydriding improves.

On the experimental side, a variety of useful approaches have been demonstrated to measure composition, phase evolution, and mass transport at surfaces and interfaces during Ti hydriding. Such quantities already provide a compelling roadmap for direct integration with theoretical calculations. Nevertheless, the development of complementary experiments capable of validating theoretically predicted phenomena at *all* relevant length scales remains challenging: single experiments usually result in a qualitative or quantitative measurement that at best corresponds to a single value within a theoretical model. Such experiments offer little help to validate theory at multiple length scales simultaneously—key to extracting reliable connections between atomistic, microstructural, and macroscale behavior—and are therefore subject to sample-to-sample variation. One way to address this problem is to prioritize development *in situ* and *in operando* methodologies capable of taking multiple measurements during the hydrogen uptake process. Ideally, the measurement modalities would be capable of quantifying multiple physical changes that span length scales (e.g., resistivity, optical properties, mass, and dilatometry, followed by imaging and destructive techniques). Having access to these simultaneous probes would provide significant value for existing efforts to integrate experiments and theory towards a deeper understanding of materials changes during hydriding.

In conclusion, we emphasize that because combined theory–experiment approaches can uniquely and holistically investigate surface morphology, chemical composition, and hydrogen transport, future investments along these lines will be crucial. Such investments, properly realized, can guide forthcoming strategies for slowing hydriding of Ti alloys in corrosion-resistant structural applications. On the opposite side of this coin, we suggest that the obtained scientific understanding could likewise be applied to accelerate hydriding Ti-based materials for emerging functional applications, including hydrogen and thermal storage.

Declaration of Competing Interest

The authors declare that they have no known competing financial interests or personal relationships that could have appeared to influence the work reported in this paper.

Data availability

Data will be made available on request.

Acknowledgements

This work was performed under the auspices of the U.S. Department of Energy by Lawrence Livermore National Laboratory under Contract DE-AC52-07NA27344. This work was funded by the Laboratory Directed Research and Development (LDRD) program (20-SI-04) at Lawrence Livermore National Laboratory. BCW and TWH acknowledge additional funding from the Hydrogen Materials—Advanced Research Consortium, provided by the U.S. Department of Energy Hydrogen and Fuel Cell Technologies Office, Office of Energy Efficiency and Renewable Energy, under Contract DE-AC52-07NA27344.

Appendix A. Supplementary material

Supplementary data to this article can be found online at https://doi.org/10.1016/j.cossms.2022.101020.

References

[1] N. Vaché, Y. Cadoret, B. Dod, D. Monceau, Modeling the oxidation kinetics of titanium alloys: Review, method and application to Ti-64 and Ti-6242s alloys, Corros. Sci. 178 (2021), 109041.
[2] L.-C. Zhang, L.-Y. Chen, A Review on Biomedical Titanium Alloys: Recent Progress and Prospect, Adv. Eng. Mater. 21 (4) (2019) 1801215.
[3] D. Zhang, D. Qiu, M.A. Gibson, Y. Zheng, H.L. Fraser, D.H. StJohn, M.A. Easton, Additive manufacturing of ultrafine-grained high-strength titanium alloys, Nature 576 (7785) (2019) 91–95.
[4] S. Bahl, S. Suwas, K. Chatterjee, Comprehensive review on alloy design, processing, and performance of β Titanium alloys as biomedical materials, Int. Mater. Rev. (2020) 1–26.
[5] D. Banerjee, J. Williams, Perspectives on titanium science and technology, Acta Mater. 61 (3) (2013) 844–879.
[6] B. Nagesha, V. Dhinakaran, M.V. Shree, K.M. Kumar, T. Jagadeesha, A review on weldability of additive manufactured titanium alloys, Mater. Today:. Proc. (2020).
[7] S. Yan, G.-L. Song, Z. Li, H. Wang, D. Zheng, F. Cao, M. Horynova, M.S. Dargusch, L. Zhou, A state-of-the-art review on passivation and biofouling of Ti and its alloys in marine environments, J. Mater. Sci. Technol. 34 (3) (2018) 421–435.
[8] R. Shi, Y. Gao, D. Li, W. Zhao, Y. Zheng, Recent Advances in the Design of Novel β-Titanium Alloys Using Integrated Theory, Computer Simulation, and Advanced Characterization, Adv. Eng. Mater. 23 (8) (2021) 2100152.
[9] H. Attar, S. Ehtemam-Haghighi, N. Soro, D. Kent, M.S. Dargusch, Additive manufacturing of low-cost porous titanium-based composites for biomedical applications: Advantages, challenges and opinion for future development, J. Alloy. Compd. 827 (2020), 154263.
[10] R. Shi, Y. Zheng, R. Banerjee, H.L. Fraser, Y. Wang, ω-Assisted α nucleation in a metastable β titanium alloy, Scr. Mater. 171 (2019) 62–66.
[11] H. Attar, M. Bermingham, S. Ehtemam-Haghighi, A. Dehghan-Manshadi, D. Kent, M. Dargusch, Evaluation of the mechanical and wear properties of titanium produced by three different additive manufacturing methods for biomedical application, Mater. Sci. Eng., A 760 (2019) 339–345.
[12] A. Khalifeh, Stress Corrosion Cracking Behavior of Materials, Engineering Failure Analysis, IntechOpen2020.
[13] F. Hua, K. Mon, P. Pasupathi, G. Gordon, D. Shoesmith, A review of corrosion of titanium grade 7 and other titanium alloys in nuclear waste repository environments, Corrosion 61 (10) (2005) 987–1003.
[14] S. Antonov, R. Shi, D. Li, Z. Kloenne, Y. Zheng, H.L. Fraser, D. Raabe, B. Gault, Nucleation and growth of α phase in a metastable β-Titanium Ti-5Al-5Mo-5V-3Cr alloy: Influence from the nano-scale, ordered-orthorhombic O″ phase and α compositional evolution, Scr. Mater. 194 (2021), 113672.
[15] R. Shi, S. Khairallah, T.W. Heo, M. Rolchigo, J.T. McKeown, M.J. Matthews, Integrated Simulation Framework for Additively Manufactured Ti-6Al-4V: Melt Pool Dynamics, Microstructure, Solid-State Phase Transformation, and Microelastic Response, JOM 71 (10) (2019) 3640–3655.
[16] I. Polmear, D. StJohn, J.-F. Nie, M. Qian, Light alloys: metallurgy of the light metals, Butterworth-Heinemann2017.
[17] Y. Liu, Z. Ren, J. Liu, R. Schaller, E. Asselin, Electrochemical Investigation and Identification of Titanium Hydrides Formed in Mixed Chloride Sulfuric Acid Solution, J. Electrochem. Soc. 166 (11) (2019) C3096.
[18] M. Vezvaie, J. Noël, Z. Tun, D. Shoesmith, Hydrogen absorption into titanium under cathodic polarization: an in-situ neutron reflectometry and EIS study, J. Electrochem. Soc. 160 (9) (2013) C414.
[19] P. Hruška, J. Čížek, J. Knapp, F. Lukáč, O. Melikhova, S. Mašková, L. Havela, J. Drahokoupil, Characterization of defects in titanium created by hydrogen charging, Int. J. Hydrogen Energy 42 (35) (2017) 22557–22563.
[20] S. Liu, Z. Zhang, J. Xia, Y. Chen, Effect of Hydrogen Precharging on Mechanical and Electrochemical Properties of Pure Titanium, Adv. Eng. Mater. 22 (5) (2020) 1901182.
[21] A. Schneemann, J.L. White, S. Kang, S. Jeong, L.F. Wan, E.S. Cho, T.W. Heo, D. Prendergast, J.J. Urban, B.C. Wood, M.D. Allendorf, V. Stavila, Nanostructured Metal Hydrides for Hydrogen Storage, Chem. Rev. 118 (22) (2018) 10775–10839.
[22] E. Tal-Gutelmacher, D. Eliezer, The hydrogen embrittlement of titanium-based alloys, Jom 57 (9) (2005) 46–49.
[23] V. Sinha, R. Schwarz, M. Mills, J. Williams, Effects of hydrogen on fatigue behavior of near-alpha titanium alloys, Scr. Mater. 153 (2018) 81–85.
[24] Q. Wang, S. Xu, J.-S. Lecomte, C. Schuman, L. Peltier, X. Shen, W. Song, Crystallographic orientation dependence of hydride precipitation in commercial pure titanium, Acta Mater. 183 (2020) 329–339.
[25] J. Vaughan, P. Reid, A. Alfantazi, Corrosion of Ti-2 and Ti-7 relevant to nickel acid leach chemistry, Hydrometallurgy 101 (3–4) (2010) 156–165.
[26] M.O. Bodunrin, L.H. Chown, J.W. van der Merwe, K.K. Alaneme, C. Oganbule, D. E. Klenam, N.P. Mphasha, Corrosion behavior of titanium alloys in acidic and saline media: role of alloy design, passivation integrity, and electrolyte modification, Corros. Rev. 38 (1) (2020) 25–47.
[27] L. Yan, J. Noël, D. Shoesmith, Hydrogen absorption into Grade-2 titanium during crevice corrosion, Electrochim. Acta 56 (4) (2011) 1810–1822.
[28] Y. Zeng, J. Noël, P. Norton, D. Shoesmith, Hydrogen transport through thin titanium oxides, J. Electroanal. Chem. 649 (1–2) (2010) 277–285.
[29] E. Vermesse, C. Mabru, L. Arurault, Surface integrity after pickling and anodization of Ti–6Al–4V titanium alloy, Appl. Surf. Sci. 285 (2013) 629–637.
[30] J. Kim, C.C. Tasan, Microstructural and micro-mechanical characterization during hydrogen charging: An in situ scanning electron microscopy study, Int. J. Hydrogen Energy 44 (12) (2019) 6333–6343.
[31] J. Kim, E. Plancher, C.C. Tasan, Hydrogenation-induced lattice expansion and its effects on hydrogen diffusion and damage in Ti–6Al–4V, Acta Mater. 188 (2020) 686–696.
[32] P.A. Olsson, M. Mrovec, M. Kroon, First principles characterisation of brittle transgranular fracture of titanium hydrides, Acta Mater. 118 (2016) 362–373.
[33] Y. Chang, A.J. Breen, Z. Tarzimoghadam, P. Kürnsteiner, H. Gardner, A. Ackerman, A. Radecka, P.A. Bagot, W. Lu, T. Li, Characterizing solute

hydrogen and hydrides in pure and alloyed titanium at the atomic scale, Acta Mater. 150 (2018) 273–280.
[34] Y. Chang, W. Lu, J. Guénolé, L.T. Stephenson, A. Szczpaniak, P. Kontis, A. K. Ackerman, F.F. Dear, I. Mouton, X. Zhong, Ti and its alloys as examples of cryogenic focused ion beam milling of environmentally-sensitive materials, Nat. Commun. 10 (1) (2019) 1–10.
[35] R. Traylor, R. Zhang, J. Kacher, J.O. Douglas, P.A. Bagot, A.M. Minor, Impurity and texture driven HCP-to-FCC transformations in Ti-X thin films during in situ TEM annealing and FIB milling, Acta Mater. 184 (2020) 199–210.
[36] A. Ulvestad, M. Welland, S. Collins, R. Harder, E. Maxey, J. Wingert, A. Singer, S. Hy, P. Mulvaney, P. Zapol, Avalanching strain dynamics during the hydriding phase transformation in individual palladium nanoparticles, Nat. Commun. 6 (1) (2015) 1–8.
[37] A. Ulvestad, A. Yau, The self-healing of defects induced by the hydriding phase transformation in palladium nanoparticles, Nat. Commun. 8 (1) (2017) 1–6.
[38] H. Luo, Z. Li, Y.-H. Chen, D. Ponge, M. Rohwerder, D. Raabe, Hydrogen effects on microstructural evolution and passive film characteristics of a duplex stainless steel, Electrochem. Commun. 79 (2017) 28–32.
[39] S. Evers, M. Rohwerder, The hydrogen electrode in the “dry”: A Kelvin probe approach to measuring hydrogen in metals, Electrochem. Commun. 24 (2012) 85–88.
[40] C. Senöz, S. Evers, M. Stratmann, M. Rohwerder, Scanning Kelvin probe as a highly sensitive tool for detecting hydrogen permeation with high local resolution, Electrochem. Commun. 13 (12) (2011) 1542–1545.
[41] M. Rohwerder, F. Turcu, High-resolution Kelvin probe microscopy in corrosion science: scanning Kelvin probe force microscopy (SKPFM) versus classical scanning Kelvin probe (SKP), Electrochim. Acta 53 (2) (2007) 290–299.
[42] S. Evers, C. Senöz, M. Rohwerder, Hydrogen detection in metals: a review and introduction of a Kelvin probe approach, Sci. Technol. Adv. Mater. 14 (1) (2013), 014201.
[43] M. Koyama, A. Bashir, M. Rohwerder, S.V. Merzlikin, E. Akiyama, K. Tsuzaki, D. Raabe, Spatially and kinetically resolved mapping of hydrogen in a twinning-induced plasticity steel by use of scanning Kelvin probe force microscopy, J. Electrochem. Soc. 162 (12) (2015) C638.
[44] E. Tohme, V. Barnier, F. Christien, C. Bosch, K. Wolski, M. Zamanzade, SKPFM study of hydrogen in a two phase material. Experiments and modelling, Int. J. Hydrogen Energy 44 (33) (2019) 18597–18605.
[45] W. Krieger, S.V. Merzlikin, A. Bashir, A. Szczepaniak, H. Springer, M. Rohwerder, Spatially resolved localization and characterization of trapped hydrogen in zero to three dimensional defects inside ferritic steel, Acta Mater. 144 (2018) 235–244.
[46] G. Wang, Y. Yan, X. Yang, J. Li, L. Qiao, Investigation of hydrogen evolution and enrichment by scanning Kelvin probe force microscopy, Electrochem. Commun. 35 (2013) 100–103.
[47] P. Olsson, J. Blomqvist, C. Bjerkén, A. Massih, Ab initio thermodynamics investigation of titanium hydrides, Comput. Mater. Sci. 97 (2015) 263–275.
[48] G. Leyson, B. Grabowski, J. Neugebauer, Multiscale modeling of hydrogen enhanced homogeneous dislocation nucleation, Acta Mater. 107 (2016) 144–151.
[49] G. Leyson, B. Grabowski, J. Neugebauer, Multiscale description of dislocation induced nano-hydrides, Acta Mater. 89 (2015) 50–59.
[50] T.W. Heo, K.B. Colas, A.T. Motta, L.-Q. Chen, A phase-field model for hydride formation in polycrystalline metals: Application to δ-hydride in zirconium alloys, Acta Mater. 181 (2019) 262–277.
[51] B.C. Wood, T.W. Heo, S. Kang, L.F. Wan, S. Li, Beyond Idealized Models of Nanoscale Metal Hydrides for Hydrogen Storage, Ind. Eng. Chem. Res. 59 (13) (2020) 5786–5796.
[52] J. Ai, Y. Chen, M. Urquidi-Macdonald, D.D. Macdonald, Electrochemical impedance spectroscopic study of passive zirconium: I. High-temperature, deaerated aqueous solutions, J. Electrochem. Soc. 154 (1) (2006) C43.
[53] J. Ai, Y. Chen, M. Urquidi-Macdonald, D.D. Macdonald, Electrochemical Impedance Spectroscopic Study of Passive Zirconium: II. High-Temperature, Hydrogenated Aqueous Solutions, J. Electrochem. Soc. 154 (1) (2006) C52.
[54] J. Henderson, N. Ebrahimi, V. Dehnavi, M. Guo, D. Shoesmith, J. Noël, The role of internal cathodic support during the crevice corrosion of Ni-Cr-Mo alloys, Electrochim. Acta 283 (2018) 1600–1608.
[55] R. Zhu, C. Nowierski, Z. Ding, J.J. Noël, D.W. Shoesmith, Insights into Grain Structures and Their Reactivity on Grade-2 Ti Alloy Surfaces by Scanning Electrochemical Microscopy, Chem. Mater. 19 (10) (2007) 2533–2543.
[56] R.W. Schutz, Corrosion of titanium and titanium alloys, ASM Handbook, Vol. 13 B, Corrosion: Materials 13 (2005) 252-299.
[57] Z. Wang, C. Briant, K. Kumar, Hydrogen embrittlement of grade 2 and grade 3 titanium in 6% sodium chloride solution, Corrosion 54 (7) (1998) 553–560.
[58] L. Yan, S. Ramamurthy, J. Noël, D. Shoesmith, Hydrogen absorption into alpha titanium in acidic solutions, Electrochim. Acta 52 (3) (2006) 1169–1181.
[59] O. Abdul-Hamid, R. Latanision, Diffusion of hydrogen in titanium, Hydrogen Effects in Materials; John Wiley & Sons, Inc.: Hoboken, NJ, USA (2013) 205-214.
[60] N. Pushilina, M. Syrtanov, E. Kashkarov, T. Murashkina, V. Kudiiarov, R. Laptev, A. Lider, A. Koptyug, Influence of manufacturing parameters on microstructure and hydrogen sorption behavior of electron beam melted titanium Ti-6Al-4V alloy, Materials 11 (5) (2018) 763.
[61] N. Pushilina, A. Panin, M. Syrtanov, E. Kashkarov, V. Kudiiarov, O. Perevalova, R. Laptev, A. Lider, A. Koptyug, Hydrogen-induced phase transformation and microstructure evolution for Ti-6Al-4V parts produced by electron beam melting, Metals 8 (5) (2018) 301.
[62] R. Silverstein, D. Eliezer, Hydrogen trapping in 3D-printed (additive manufactured) Ti-6Al-4V, Mater. Charact. 144 (2018) 297–304.
[63] R. Laptev, V. Kudiiarov, N. Pushilina, Hydrogen influence on defect structure and mechanical properties of EBM Ti-6Al-4V, Mater. Today:. Proc. 19 (2019) 2084–2088.
[64] S. Woods, J.A. Lee, Hydrogen embrittlement, (2016).
[65] R. Singh, R. Kishore, S. Mukherjee, S. Roychowdhury, D. Srivastava, T. Sinha, P. De, S. Banerjee, B. Gopalan, R. Kameswaran, Hydrogen charging, hydrogen content analysis and metallographic examination of hydride in Zirconium alloys, Bhabha Atomic Research Centre (2003).
[66] T. Suda, M. Ohkawa, S. Sawada, S. Watanabe, S. Ohnuki, S. Nagata, Effect of surface modification by ion implantation on hydrogenation property of TiFe alloy, Mater. Trans. 43 (11) (2002) 2703–2705.
[67] A. López-Suárez, C. Valencia, J. López-Patiño, M. Vargas, B. Fuentes, Improvement of titanium hydrogenation by low energy ion irradiation, Int. J. Hydrogen Energy 40 (11) (2015) 4194–4199.
[68] T. Wang, D. Grambole, R. Grötzschel, F. Herrmann, U. Kreißig, F. Eichhorn, G. Brauer, W. Möller, Mobility and retention of implanted hydrogen in Ti225 titanium alloy, Surf. Coat. Technol. 158 (2002) 139–145.
[69] A. López-Suárez, N. García-Zúñiga, Study of hydrogen storage capacity of Ti induced by ion irradiation, Int. J. Hydrogen Energy 42 (20) (2017) 14199–14204.
[70] J.G. Novaković, L. Matović, M. Drvendžija, N. Novaković, D. Rajnović, M. Šiljegović, Z.K. Popović, S. Milovanović, N. Ivanović, Changes of hydrogen storage properties of MgH2 induced by heavy ion irradiation, Int. J. Hydrogen Energy 33 (7) (2008) 1876–1879.
[71] H. Abe, S. Aone, R. Morimoto, H. Uchida, T. Ohshima, Improvement of hydrogen absorption characteristics of Pd using irradiation of heavy ions, Trans. Mater. Res. Soc. Jpn 36 (1) (2011) 133–135.
[72] N.U. Navi, J. Tenenbaum, E. Sabatani, G. Kimmel, R.B. David, B.A. Rosen, Z. Barkay, V. Ezersky, E. Tiferet, Y.I. Ganor, Hydrogen effects on electrochemically charged additive manufactured by electron beam melting (EBM) and wrought Ti–6Al–4V alloys, Int. J. Hydrogen Energy 45 (46) (2020) 25523–25540.
[73] K. Verbeken, Analysing hydrogen in metals: bulk thermal desorption spectroscopy (TDS) methods, Gaseous hydrogen embrittlement of materials in energy technologies, Elsevier (2012) 27–55.
[74] K. Azumi, Y. Asada, T. Ueno, M. Seo, T. Mizuno, Monitoring of hydrogen absorption into titanium using resistometry, J. Electrochem. Soc. 149 (9) (2002) B422.
[75] X. He, J.J. Noël, D.W. Shoesmith, Temperature dependence of crevice corrosion initiation on titanium grade-2, J. Electrochem. Soc. 149 (9) (2002) B440.
[76] G.R. Caskey, Diffusion of tritium in rutile (TiO2), Materials Science and Engineering 14 (2) (1974) 109–114.
[77] W. Mao, M. Wilde, S. Ogura, J. Chen, K. Fukutani, H. Matsuzaki, T. Terai, Hydrogen-Accelerated Phase Transition and Diffusion in TiO2 Thin Films, The Journal of Physical Chemistry C 122 (40) (2018) 23026–23033.
[78] S. Yen, Retardation effects of thermally grown oxide films on the hydrogen embrittlement of commercial pure titanium, Corros. Sci. 41 (10) (1999) 2031–2051.
[79] R. Zhu, Z. Qin, J.J. Noël, D.W. Shoesmith, Z. Ding, Analyzing the influence of alloying elements and impurities on the localized reactivity of titanium grade-7 by scanning electrochemical microscopy, Anal. Chem. 80 (5) (2008) 1437–1447.
[80] N. Makivic, J.-Y. Cho, K.D. Harris, J.-M. Tarascon, B. Limoges, V. Balland, Evidence of Bulk Proton Insertion in Nanostructured Anatase and Amorphous TiO2 Electrodes, Chem. Mater. 33 (9) (2021) 3436–3448.
[81] M. Hannula, H. Ali-Löytty, K. Lahtonen, E. Sarlin, J. Saari, M. Valden, Improved stability of atomic layer deposited amorphous TiO2 photoelectrode coatings by thermally induced oxygen defects, Chem. Mater. 30 (4) (2018) 1199–1208.
[82] M.M. Islam, M. Calatayud, G. Pacchioni, Hydrogen Adsorption and Diffusion on the Anatase TiO2(101) Surface: A First-Principles Investigation, The Journal of Physical Chemistry C 115 (14) (2011) 6809–6814.
[83] U. Aschauer, A. Selloni, Hydrogen interaction with the anatase TiO2(101) surface, PCCP 14 (48) (2012) 16595–16602.
[84] P. Raghunath, W.F. Huang, M.C. Lin, Quantum chemical elucidation of the mechanism for hydrogenation of TiO2 anatase crystals, J. Chem. Phys. 138 (15) (2013), 154705.
[85] P.F. Chester, D.H. Bradhurst, Electrolytically Induced Conductivity in Rutile, Nature 199 (4898) (1963) 1056–1057.
[86] P. Sundaram, E. Wessel, H. Clemens, H. Kestler, P. Ennis, W. Quadakkers, L. Singheiser, Determination of the diffusion coefficient of hydrogen in gamma titanium aluminides during electrolytic charging, Acta Mater. 48 (5) (2000) 1005–1019.
[87] H.-J. Christ, M. Decker, S. Zeitler, Hydrogen diffusion coefficients in the titanium alloys IMI 834, Ti 10-2-3, Ti 21 S, and alloy C, Metallurgical and Materials Transactions A 31 (6) (2000) 1507–1517.
[88] M. Hein, A. Bals, A. Privalov, H. Wipf, Gorsky effect study of H and D diffusion in V and Ti at high H (D) concentrations, J. Alloy. Compd. 356 (2003) 318–321.
[89] I. Novoselov, A. Yanilkin, Hydrogen diffusion in titanium dihydrides from first principles, Acta Mater. 153 (2018) 250–256.
[90] S. Frappart, A. Oudriss, X. Feaugas, J. Creus, J. Bouhattate, F. Thébault, L. Delattre, H. Marchebois, Hydrogen trapping in martensitic steel investigated using electrochemical permeation and thermal desorption spectroscopy, Scr. Mater. 65 (10) (2011) 859–862.
[91] S. Teus, D. Savvakin, O. Ivasishin, V. Gavriljuk, Hydrogen migration and hydrogen-dislocation interaction in austenitic steels and titanium alloy in relation to hydrogen embrittlement, Int. J. Hydrogen Energy 42 (4) (2017) 2424–2433.

[92] M. Wang, E. Akiyama, K. Tsuzaki, Effect of hydrogen on the fracture behavior of high strength steel during slow strain rate test, Corros. Sci. 49 (11) (2007) 4081–4097.
[93] W. Counts, C. Wolverton, R. Gibala, First-principles energetics of hydrogen traps in α-Fe: Point defects, Acta Mater. 58 (14) (2010) 4730–4741.
[94] S. Taketomi, R. Matsumoto, N. Miyazaki, Atomistic study of hydrogen distribution and diffusion around a {1 1 2}< 1 1 1> edge dislocation in alpha iron, Acta Mater. 56 (15) (2008) 3761–3769.
[95] V. Ramunni, T.D.P. Coelho, P.V. de Miranda, Interaction of hydrogen with the microstructure of low-carbon steel, Mater. Sci. Eng., A 435 (2006) 504–514.
[96] A. Nagao, M.L. Martin, M. Dadfarnia, P. Sofronis, I.M. Robertson, The effect of nanosized (Ti, Mo) C precipitates on hydrogen embrittlement of tempered lath martensitic steel, Acta Mater. 74 (2014) 244–254.
[97] F.-G. Wei, T. Hara, K. Tsuzaki, Nano-preciptates design with hydrogen trapping character in high strength steel, Advanced steels, Springer2011, pp. 87-92.
[98] S. Frappart, X. Feaugas, J. Creus, F. Thebault, L. Delattre, H. Marchebois, Study of the hydrogen diffusion and segregation into Fe–C–Mo martensitic HSLA steel using electrochemical permeation test, J. Phys. Chem. Solids 71 (10) (2010) 1467–1479.
[99] I.H. Katzarov, D.L. Pashov, A.T. Paxton, Hydrogen embrittlement I. Analysis of hydrogen-enhanced localized plasticity: Effect of hydrogen on the velocity of screw dislocations in α-Fe, Physical Review Materials 1 (3) (2017), 033602.
[100] M. Itakura, H. Kaburaki, M. Yamaguchi, T. Okita, The effect of hydrogen atoms on the screw dislocation mobility in bcc iron: A first-principles study, Acta Mater. 61 (18) (2013) 6857–6867.
[101] H. Yu, A. Cocks, E. Tarleton, Discrete dislocation plasticity HELPs understand hydrogen effects in bcc materials, J. Mech. Phys. Solids 123 (2019) 41–60.
[102] Y.-H. Li, H.-B. Zhou, F. Gao, G. Lu, G.-H. Lu, F. Liu, Hydrogen induced dislocation core reconstruction in bcc tungsten, Acta Mater. 226 (2022), 117622.
[103] P.M. Anderson, J.P. Hirth, J. Lothe, Theory of dislocations, Cambridge University Press2017.
[104] G. Lu, Q. Zhang, N. Kioussis, E. Kaxiras, Hydrogen-enhanced local plasticity in aluminum: an ab initio study, Phys. Rev. Lett. 87 (9) (2001), 095501.
[105] D. Wang, X. Lu, Y. Deng, X. Guo, A. Barnoush, Effect of hydrogen on nanomechanical properties in Fe-22Mn-0.6 C TWIP steel revealed by in-situ electrochemical nanoindentation, Acta Mater. 166 (2019) 618–629.
[106] X. Lu, D. Wang, D. Wan, Z. Zhang, N. Kheradmand, A. Barnoush, Effect of electrochemical charging on the hydrogen embrittlement susceptibility of alloy 718, Acta Mater. 179 (2019) 36–48.
[107] Y. Deng, A. Barnoush, Hydrogen embrittlement revealed via novel in situ fracture experiments using notched micro-cantilever specimens, Acta Mater. 142 (2018) 236–247.
[108] K. Zhao, J. He, A. Mayer, Z. Zhang, Effect of hydrogen on the collective behavior of dislocations in the case of nanoindentation, Acta Mater. 148 (2018) 18–27.
[109] A. Tehranchi, W.A. Curtin, The role of atomistic simulations in probing hydrogen effects on plasticity and embrittlement in metals, Eng. Fract. Mech. 216 (2019), 106502.
[110] S. Yin, G. Cheng, T.-H. Chang, G. Richter, Y. Zhu, H. Gao, Hydrogen embrittlement in metallic nanowires, Nat. Commun. 10 (1) (2019) 1–9.
[111] X. Lu, D. Wang, Effect of hydrogen on deformation behavior of Alloy 725 revealed by in-situ bi-crystalline micropillar compression test, J Mater Sci Technol 67 (2020) 243–253.
[112] A. Rokhmanenkov, A.Y. Kuksin, A. Yanilkin, Simulation of hydrogen diffusion in TiH x structures, Phys. Met. Metall. 118 (1) (2017) 28–38.
[113] G. Bond, I. Robertson, H. Birnbaum, The influence of hydrogen on deformation and fracture processes in high-strength aluminum alloys, Acta Metall. 35 (9) (1987) 2289–2296.
[114] G. Bond, I. Robertson, H. Birnbaum, On the mechanisms of hydrogen embrittlement of Ni3Al alloys, Acta Metall. 37 (5) (1989) 1407–1413.
[115] P. Ferreira, I. Robertson, H. Birnbaum, Hydrogen effects on the interaction between dislocations, Acta Mater. 46 (5) (1998) 1749–1757.
[116] J. Chateau, D. Delafosse, T. Magnin, Numerical simulations of hydrogen–dislocation interactions in fcc stainless steels.: part II: hydrogen effects on crack tip plasticity at a stress corrosion crack, Acta Mater. 50 (6) (2002) 1523–1538.
[117] R. Kirchheim, Reducing grain boundary, dislocation line and vacancy formation energies by solute segregation. I. Theoretical background, Acta Mater. 55 (15) (2007) 5129–5138.
[118] A. Barnoush, H. Vehoff, Recent developments in the study of hydrogen embrittlement: Hydrogen effect on dislocation nucleation, Acta Mater. 58 (16) (2010) 5274–5285.
[119] W. Xie, X. Liu, W. Chen, H. Zhang, Hydrogen hardening effect in heavily deformed single crystal α-Fe, Comput. Mater. Sci. 50 (12) (2011) 3397–3402.
[120] J. Song, W. Curtin, A nanoscale mechanism of hydrogen embrittlement in metals, Acta Mater. 59 (4) (2011) 1557–1569.
[121] S.M. Myers, M. Baskes, H. Birnbaum, J.W. Corbett, G. DeLeo, S. Estreicher, E. E. Haller, P. Jena, N.M. Johnson, R. Kirchheim, Hydrogen interactions with defects in crystalline solids, Rev. Mod. Phys. 64 (2) (1992) 559.
[122] D. Teter, I. Robertson, H. Birnbaum, The effects of hydrogen on the deformation and fracture of β-titanium, Acta Mater. 49 (20) (2001) 4313–4323.
[123] L. Sun, W. Xiao, S. Huang, J. Wang, L. Wang, Improving the mechanical processing of titanium by hydrogen doping: A first-principles study, Int. J. Hydrogen Energy 43 (13) (2018) 6756–6764.
[124] D.O. Poletaev, D.A. Aksyonov, D.D. Vo, A.G. Lipnitskii, Hydrogen solubility in hcp titanium with the account of vacancy complexes and hydrides: A DFT study, Comput. Mater. Sci. 114 (2016) 199–208.
[125] N.J. Lane, S.I. Simak, A.S. Mikhaylushkin, I.A. Abrikosov, L. Hultman, M. W. Barsoum, First-principles study of dislocations in hcp metals through the investigation of the ($11\overline{2}1$) twin boundary, Physical Review B 84 (18) (2011), 184101.
[126] Y. Jia, S. Hu, X. Zhou, S. Peng, Interactions between hydrogen and the (11$\bar{2}$1) twin boundary in hexagonal close-packed titanium, Int. J. Hydrogen Energy 45 (16) (2020) 9854–9864.
[127] J. Wen, N. Allain, E. Fleury, Hydrogen evolution and its effects on cold rolling behavior in commercial pure titanium, Mater. Charact. 121 (2016) 139–148.
[128] J. Wen, N. Main, E. Fleury, The Effect of Hydrogen-Deformation Interactions on Recrystallization of β-21S Titanium Alloys, Proceedings of the 13th World Conference on Titanium, Wiley Online Library, 2016, pp. 275-280.
[129] S. Wang, F. Giuliani, T.B. Britton, Microstructure and formation mechanisms of δ-hydrides in variable grain size Zircaloy-4 studied by electron backscatter diffraction, Acta Mater. 169 (2019) 76–87.
[130] T. Watanabe, T. Shindo, H. Naito, Effect of iron content on the breakdown potential for pitting of titanium in NaCl solutions, Sixth World Conference on Titanium. IV (1988) 1735–1740.
[131] F. Hua, P. Pasupathi, K. Mon, G. Gordon, D. Shoesmith, Modeling the hydrogen-induced cracking of titanium alloys in nuclear waste repository environments, JOM 57 (1) (2005) 20–26.
[132] S.K. Nayak, C.J. Hung, V. Sharma, S.P. Alpay, A.M. Dongare, W.J. Brindley, R. J. Hebert, Insight into point defects and impurities in titanium from first principles, npj Comput. Mater. 4 (1) (2018) 11.
[133] X. He, J. Noel, D. Shoesmith, Effects of iron content on microstructure and crevice corrosion of grade-2 titanium, Corrosion 60 (4) (2004) 378–386.
[134] B. Ikeda, M. Quinn, A Preliminary Examination of the Effects of Hydrogen on the Behaviour of Grade-16 Titanium at Room Temperature, Ontario Hydro (1998).
[135] B. Ikeda, M. Quinn, Hydrogen Assisted Cracking of Grade-16 Titanium: A Preliminary Examination of Behaviour at Room Temperature, Ontario Hydro (1998).
[136] D.W. Shoesmith, B.M. Ikeda, The resistance of titanium to pitting, microbially induced corrosion and corrosion in unsaturated conditions, Atomic Energy of Canada Limited (1997).
[137] G. Hubler, E. McCafferty, The corrosion behaviour and rutherford backscattering analysis of palladium-implanted titanium, Corros. Sci. 20 (1) (1980) 103–116.
[138] R. Armstrong, R. Firman, H. Thirsk, Ring-disc studies of titanium-palladium alloy corrosion, Corros. Sci. 13 (6) (1973) 409–420.
[139] T. Okada, Factors influencing the cathodic charging efficiency of hydrogen by modified titanium electrodes, Electrochim. Acta 28 (8) (1983) 1113–1120.
[140] R.S. Glass, Effect of intermetallic Ti2Ni on the electrochemistry of TiCode-12 in hydrochloric acid, Electrochim. Acta 28 (11) (1983) 1507–1513.
[141] L. Covington, R. Schutz, Effects of iron on the corrosion resistance of titanium, Industrial Applications of Titanium and Zirconium, ASTM International1981.
[142] B.M. Ikeda, M.G. Bailey, M.J. Quinn, D.W. Shoesmith, The development of an experimental data base for the lifetime predictions of titanium nuclear waste containers, Application of Accelerated Corrosion Tests to Service Life Prediction of Materials, ASTM International1994.
[143] G. Lutjering, U. Zwicker, W. Bunk, Titanium: Science and Technology: Proceedings of the Fifth International Conference on Titanium Congress-Center, Munich, FRG September 10-14, 1984, Deutsche Gesellschaft fur Metallkunde e V.1985.
[144] D. Pletcher, R. Greff, R. Peat, L. Peter, J. Robinson, Instrumental methods in electrochemistry, Elsevier2001.
[145] T. Fukuzuka, K. Shimogori, H. Satoh, Role of palladium in hydrogen absorption of Ti-Pd alloy, CORROSION ENGINEERING 29 (12) (1980) 622–628.
[146] J. Cotton, Using Titanium in the Chemical Plant, Chem. Eng. Prog. 66 (1970) 57–62.
[147] J. Wu, Effect of Iron Content on Hydrogen Absorption and Passivity Breakdown of Commercially Pure Titanium in Aqueous Solutions, Titanium-Science and Technology. 4 (1984) 2595–2602.
[148] Y. Zhu, K. Sun, G.S. Frankel, Intermetallic Phases in Aluminum Alloys and Their Roles in Localized Corrosion, J. Electrochem. Soc. 165 (11) (2018) C807–C820.
[149] Y. Zhu, D.A. Cullen, S. Kar, M.L. Free, L.F. Allard, Evaluation of Al3Mg2 Precipitates and Mn-Rich Phase in Aluminum-Magnesium Alloy Based on Scanning Transmission Electron Microscopy Imaging, Metallurgical and Materials Transactions A 43 (13) (2012) 4933–4939.
[150] Y. Zhu, J.D. Poplawsky, S. Li, R.R. Unocic, L.G. Bland, C.D. Taylor, J.S. Locke, E. A. Marquis, G.S. Frankel, Localized corrosion at nm-scale hardening precipitates in Al-Cu-Li alloys, Acta Mater. 189 (2020) 204–213.
[151] M. Topic, L. Pichon, S. Nsengiyumva, G. Favaro, M. Dubuisson, S. Halindintwali, S. Mazwi, J. Sibanyoni, C. Mtshali, K. Corin, The effect of surface oxidation on hydrogen absorption in Ti-6Al-4V alloy studied by elastic recoil detection (ERD), X-ray diffraction and nanohardness techniques, J. Alloy. Compd. 740 (2018) 879–886.
[152] E. Conforto, D. Caillard, A fast method for determining favourable orientation relationships and interface planes: Application to titanium–titanium hydrides transformations, Acta Mater. 55 (3) (2007) 785–798.
[153] E. Conforto, D. Caillard, Edge-to-edge matching at Ti-TiH interfaces: kinetics of hydride growth and clustering of precipitates with different orientation relationships, Solid State Phenomena, Trans Tech Publ, 2011, pp. 242-247.
[154] P. Millenbach, M. Givon, The electrochemical formation of titanium hydride, Journal of the less common metals 87 (2) (1982) 179–184.
[155] H. Numakura, M. Koiwa, H. Asano, H. Murata, F. Izumi, X-ray diffraction study on the formation of γ titanium hydride, Scr. Metall. 20 (2) (1986) 213–216.

[156] H.R.Z. Sandim, B.V. Morante, P.A. Suzuki, Kinetics of thermal decomposition of titanium hydride powder using in situ high-temperature X-ray diffraction (HTXRD), Mater. Res. 8 (3) (2005) 293–297.
[157] F. Manchester, A. San-Martin, H-Ti(hydrogen-titanium), Phase Diagrams of Binary Hydrogen Alloys. ASM International, Member/Customer Service Center, Materials Park, OH 44073-0002, USA, 2000. (2000) 238-258.
[158] H. Numakura, M. Koiwa, H. Asano, F. Izumi, Neutron diffraction study of the metastable γ titanium deuteride, Acta Metall. 36 (8) (1988) 2267–2273.
[159] X. Li, J. Jiang, S. Wang, J. Chen, Y. Wang, Effect of hydrogen on the microstructure and superplasticity of Ti-55 alloy, Int. J. Hydrogen Energy 42 (9) (2017) 6338–6349.
[160] X. Zheng, M. Gong, T. Xiong, H. Ge, L. Yang, Y. Zhou, S. Zheng, J. Wang, X. Ma, Deformation induced FCC lamellae and their interaction in commercial pure Ti, Scr. Mater. 162 (2019) 326–330.
[161] Y. Chang, S. Zhang, C.H. Liebscher, D. Dye, D. Ponge, C. Scheu, G. Dehm, D. Raabe, B. Gault, W. Lu, Could face-centered cubic titanium in cold-rolled commercially-pure titanium only be a Ti-hydride? Scr. Mater. 178 (2020) 39–43.
[162] Q. Yu, J. Kacher, C. Gammer, R. Traylor, A. Samanta, Z. Yang, A.M. Minor, In situ TEM observation of FCC Ti formation at elevated temperatures, Scr. Mater. 140 (2017) 9–12.
[163] S.M. Hanlon, S.Y. Persaud, F. Long, A. Korinek, M.R. Daymond, A solution to FIB induced artefact hydrides in Zr alloys, J. Nucl. Mater. 515 (2019) 122–134.
[164] I. Mouton, Y. Chang, P. Chakraborty, S. Wang, L.T. Stephenson, T. Ben Britton, B. Gault, Hydride growth mechanism in zircaloy-4: Investigation of the partitioning of alloying elements, Materialia 15 (2021), 101006.
[165] D. Haley, S.V. Merzlikin, P. Choi, D. Raabe, Atom probe tomography observation of hydrogen in high-Mn steel and silver charged via an electrolytic route, international journal of hydrogen energy 39 (23) (2014) 12221–12229.
[166] A.J. Breen, L.T. Stephenson, B. Sun, Y. Li, O. Kasian, D. Raabe, M. Herbig, B. Gault, Solute hydrogen and deuterium observed at the near atomic scale in high-strength steel, Acta Mater. 188 (2020) 108–120.
[167] A. Lanin, I. Zalivin, V. Turchin, E. Bojko, Mechanical properties of zirconium, titanium and yttrium hydride alloys, Probl. Prochn. (1984) 83–88.
[168] G. Welsch, R. Boyer, E. Collings, Materials properties handbook: titanium alloys, ASM international1993.
[169] L. Simpson, C. Cann, Fracture toughness of zirconium hydride and its influence on the crack resistance of zirconium alloys, J. Nucl. Mater. 87 (2–3) (1979) 303–316.
[170] G. Lütjering, J.C. Williams, Titanium, Springer Science & Business Media2007.
[171] C. Chen, S. Li, H. Zheng, L. Wang, K. Lu, An investigation on structure, deformation and fracture of hydrides in titanium with a large range of hydrogen contents, Acta Mater. 52 (12) (2004) 3697–3706.
[172] J. Xu, H. Cheung, S. Shi, Mechanical properties of titanium hydride, J. Alloy. Compd. 436 (1–2) (2007) 82–85.
[173] C. Chen, S. Li, K. Lu, The deformation behaviors of gamma hydrides in titanium under cyclic straining, Acta Mater. 51 (4) (2003) 931–942.
[174] D. Setoyama, J. Matsunaga, H. Muta, M. Uno, S. Yamanaka, Mechanical properties of titanium hydride, J. Alloy. Compd. 381 (1–2) (2004) 215–220.
[175] H. Numakura, M. Koiwa, Hydride precipitation in titanium, Perspectives in Hydrogen in Metals, Elsevier (1986) 501–509.
[176] Q. Xu, A. Van der Ven, First-principles investigation of metal-hydride phase stability: The Ti-H system, Physical Review B 76 (6) (2007), 064207.
[177] C. Liang, H. Gong, Atomic structure, mechanical quality, and thermodynamic property of TiH x phases, J. Appl. Phys. 114 (4) (2013), 043510.
[178] R. Cowley, Acoustic phonon instabilities and structural phase transitions, Physical Review B 13 (11) (1976) 4877.
[179] J. Liang, Y. Dai, L. Yang, S. Peng, K. Fan, X. Long, X. Zhou, X. Zu, F. Gao, Ab initio study of helium behavior in titanium tritides, Comput. Mater. Sci. 69 (2013) 107–112.
[180] Y. Fukai, The metal-hydrogen system: basic bulk properties, Springer Science & Business Media2006.
[181] W. Wolf, P. Herzig, First-principles investigations of transition metal dihydrides, TH2: T= Sc, Ti, V, Y, Zr, Nb; energetics and chemical bonding, J. Phys.: Condens. Matter 12 (21) (2000) 4535.
[182] R. Quijano, R. de Coss, D.J. Singh, Electronic structure and energetics of the tetragonal distortion for TiH 2, ZrH 2, and HfH 2: A first-principles study, Physical Review B 80 (18) (2009), 184103.
[183] X. Liu, B. Tang, Y. Zhang, Ab initio calculations of structure and thermodynamic properties of tetragonal-TiH2 under high temperatures and pressures, The European Physical Journal Applied Physics 64 (1) (2013) 10201.
[184] K. Miwa, A. Fukumoto, First-principles study on 3 d transition-metal dihydrides, Physical Review B 65 (15) (2002), 155114.
[185] S. Li, Y. Wang, Z. Che, G. Liu, Y. Ren, Y. Wang, Investigations of deformation-induced δ→ ζ phase transformation in zirconium hydride by in situ high-energy X-ray diffraction, Acta Mater. 140 (2017) 168–175.
[186] C. Örnek, A. Larsson, G.S. Harlow, F. Zhang, R. Kroll, F. Carlà, H. Hussain, U. Kivisäkk, D.L. Engelberg, E. Lundgren, Metastable precursor structures in hydrogen-infused super duplex stainless steel microstructure–An operando diffraction experiment, Corros. Sci. 176 (2020), 109021.
[187] Y. Zhu, M.L. Free, R. Woollam, W. Durnie, A review of surfactants as corrosion inhibitors and associated modeling, Prog. Mater Sci. 90 (2017) 159–223.
[188] K. Videm, S. Lamolle, M. Monjo, J.E. Ellingsen, S.P. Lyngstadaas, H.J. Haugen, Hydride formation on titanium surfaces by cathodic polarization, Appl. Surf. Sci. 255 (5) (2008) 3011–3015.
[189] J. Vaughan, A. Alfantazi, Corrosion of titanium and its alloys in sulfuric acid in the presence of chlorides, J. Electrochem. Soc. 153 (1) (2005) B6.
[190] A. Revathi, S. Magesh, V.K. Balla, M. Das, G. Manivasagam, Current advances in enhancement of wear and corrosion resistance of titanium alloys-a review, Mater. Technol. 31 (12) (2016) 696–704.
[191] G. Sander, J. Tan, P. Balan, O. Gharbi, D. Feenstra, L. Singer, S. Thomas, R. Kelly, J.R. Scully, N. Birbilis, Corrosion of additively manufactured alloys: a review, Corrosion 74 (12) (2018) 1318–1350.
[192] D. Ellerbrock, D.D. Macdonald, Passivity of titanium, part 1: film growth model diagnostics, J. Solid State Electrochem. 18 (5) (2014) 1485–1493.
[193] B. Roh, D.D. Macdonald, Passivity of titanium: part II, the defect structure of the anodic oxide film, J. Solid State Electrochem. 23 (7) (2019) 1967–1979.
[194] B. Roh, D.D. Macdonald, The passivity of titanium—part III: characterization of the anodic oxide film, J. Solid State Electrochem. 23 (7) (2019) 2001–2008.
[195] B. Roh, D.D. Macdonald, Passivity of titanium, part IV: reversible oxygen vacancy generation/annihilation, J. Solid State Electrochem. 23 (10) (2019) 2863–2879.
[196] M. Martin, P. Sofronis, I. Robertson, T. Awane, Y. Murakami, A microstructural based understanding of hydrogen-enhanced fatigue of stainless steels, Int. J. Fatigue 57 (2013) 28–36.
[197] I.M. Robertson, P. Sofronis, A. Nagao, M. Martin, S. Wang, D. Gross, K. Nygren, Hydrogen embrittlement understood, Metallurgical and Materials Transactions B 46 (3) (2015) 1085–1103.
[198] R. Kirchheim, Revisiting hydrogen embrittlement models and hydrogen-induced homogeneous nucleation of dislocations, Scr. Mater. 62 (2) (2010) 67–70.
[199] S. Lynch, Hydrogen embrittlement phenomena and mechanisms, Corros. Rev. 30 (3–4) (2012) 105–123.
[200] S. Lynch, Towards understanding mechanisms and kinetics of environmentally assisted cracking, Environment-induced cracking of materials, Elsevier2008, pp. 167-177.
[201] R. Oriani, A mechanistic theory of hydrogen embrittlement of steels, Ber. Bunsenges. Phys. Chem. 76 (8) (1972) 848–857.
[202] Y. Wang, J. Gong, W. Jiang, A quantitative description on fracture toughness of steels in hydrogen gas, Int. J. Hydrogen Energy 38 (28) (2013) 12503–12508.
[203] Z. Tarzimoghadam, M. Rohwerder, S.V. Merzlikin, A. Bashir, L. Yedra, S. Eswara, D. Ponge, D. Raabe, Multi-scale and spatially resolved hydrogen mapping in a Ni–Nb model alloy reveals the role of the δ phase in hydrogen embrittlement of alloy 718, Acta Mater. 109 (2016) 69–81.
[204] M. Nagumo, Function of hydrogen in embrittlement of high-strength steels, ISIJ Int. 41 (6) (2001) 590–598.
[205] M. Nagumo, Conformity between mechanics and microscopic functions of hydrogen in failure, ISIJ Int. 52 (2) (2012) 168–173.
[206] Z. Tarzimoghadam, D. Ponge, J. Klöwer, D. Raabe, Hydrogen-assisted failure in Ni-based superalloy 718 studied under in situ hydrogen charging: the role of localized deformation in crack propagation, Acta Mater. 128 (2017) 365–374.
[207] Y. Tateyama, T. Ohno, Stability and clusterization of hydrogen-vacancy complexes in α− Fe: an ab initio study, Physical Review B 67 (17) (2003), 174105.
[208] S. Li, Y. Li, Y.-C. Lo, T. Neeraj, R. Srinivasan, X. Ding, J. Sun, L. Qi, P. Gumbsch, J. Li, The interaction of dislocations and hydrogen-vacancy complexes and its importance for deformation-induced proto nano-voids formation in α-Fe, Int. J. Plast. 74 (2015) 175–191.
[209] D. Prando, A. Brenna, M.V. Diamanti, S. Beretta, F. Bolzoni, M. Ormellese, M. Pedeferri, Corrosion of titanium: Part 1: Aggressive environments and main forms of degradation, Journal of Applied Biomaterials & Functional Materials 15 (4) (2017) e291–e302.
[210] R. Cottis, Shreir's corrosion, Elsevier Amsterdam, The Netherlands:2010.
[211] Z.D. Harris, J.A. Ronevich, V. Stavila, B.P. Somerday, On the fatigue crack growth behavior of Ti–10V–2Fe–3Al in gaseous hydrogen, Int. J. Hydrogen Energy 45 (51) (2020) 27929–27940.
[212] V. Madina, I. Azkarate, Compatibility of materials with hydrogen, Particular case: Hydrogen embrittlement of titanium alloys, International journal of hydrogen energy 34 (14) (2009) 5976–5980.
[213] S. Cao, S. Zhu, C.V.S. Lim, X. Zhou, X. Chen, B.R. Hinton, R.R. Boyer, J. C. Williams, X. Wu, The mechanism of aqueous stress-corrosion cracking of α+ β titanium alloys, Corros. Sci. 125 (2017) 29–39.
[214] S. Cao, C.V.S. Lim, B. Hinton, X. Wu, Effects of microtexture and Ti3Al (α2) precipitates on stress-corrosion cracking properties of a Ti-8Al-1Mo-1V alloy, Corros. Sci. 116 (2017) 22–33.
[215] D. Shih, I. Robertson, H. Birnbaum, Hydrogen embrittlement of α titanium: in situ TEM studies, Acta Metall. 36 (1) (1988) 111–124.
[216] J. Scully, D. Powell, The stress corrosion cracking mechanism of α-titanium alloys at room temperature, Corros. Sci. 10 (10) (1970) 719–733.
[217] S. Josepha, P. Kontis, Y. Chang, Y. Shi, D. Raabe, B. Gault, D. Dye, A cracking oxygen story: a new view of stress corrosion cracking in titanium alloys, arXiv preprint arXiv:2009.10567 (2020).
[218] D.D. Macdonald, The history of the point defect model for the passive state: a brief review of film growth aspects, Electrochim. Acta 56 (4) (2011) 1761–1772.
[219] S. Kang, L.E. Klebanoff, A.A. Baker, D.F. Cowgill, V. Stavila, J.R.I. Lee, M. H. Nielsen, K.G. Ray, Y.S. Liu, B.C. Wood, Assessing the reactivity of TiCl3 and TiF3 with hydrogen, Int. J. Hydrogen Energy 43 (31) (2018) 14507–14519.
[220] S.T. Sen-Britain, N.D. Keilbart, K.E. Kweon, T. Anh Pham, C.A. Orme, B.C. Wood, A.J. Nelson, Transformations of Ti-5Al-5V-5Cr-3Mo powder due to reuse in laser powder bed fusion: A surface analytical approach, Appl. Surf. Sci. 564 (2021), 150433.
[221] A.T. Landers, H. Peng, D.M. Koshy, S.H. Lee, J.T. Feaster, J.C. Lin, J.W. Beeman, D. Higgins, J. Yano, W.S. Drisdell, R.C. Davis, M. Bajdich, F. Abild-Pedersen, A. Mehta, T.F. Jaramillo, C. Hahn, Dynamics and Hysteresis of Hydrogen Intercalation and Deintercalation in Palladium Electrodes: A Multimodal In Situ

X-ray Diffraction, Coulometry, and Computational Study, Chemistry of Materials 33 (15) (2021) 5872–5884.
[222] T.Y. Wei, K.L. Lim, Y.S. Tseng, S.L.I. Chan, A review on the characterization of hydrogen in hydrogen storage materials, Renew. Sustain. Energy Rev. 79 (2017) 1122–1133.
[223] J.R. Greer, J.T.M. De Hosson, Plasticity in small-sized metallic systems: Intrinsic versus extrinsic size effect, Prog. Mater Sci. 56 (6) (2011) 654–724.
[224] O. Kraft, P.A. Gruber, R. Mönig, D. Weygand, Plasticity in confined dimensions, Annu. Rev. Mater. Res. 40 (2010) 293–317.
[225] D. Xie, S. Li, M. Li, Z. Wang, P. Gumbsch, J. Sun, E. Ma, J. Li, Z. Shan, Hydrogenated vacancies lock dislocations in aluminium, Nat. Commun. 7 (1) (2016) 1–7.
[226] T. Hajilou, M.S. Hope, A.H. Zavieh, N. Kheradmand, R. Johnsen, A. Barnoush, In situ small-scale hydrogen embrittlement testing made easy: An electrolyte for preserving surface integrity at nano-scale during hydrogen charging, Int. J. Hydrogen Energy 43 (27) (2018) 12516–12529.
[227] I. Gutierrez-Urrutia, S. Zaefferer, D. Raabe, Coupling of Electron Channeling with EBSD: Toward the Quantitative Characterization of Deformation Structures in the SEM, JOM 65 (9) (2013) 1229–1236.
[228] S. Han, P. Eisenlohr, M.A. Crimp, ECCI based characterization of dislocation shear in polycrystalline arrays during heterogeneous deformation of commercially pure titanium, Mater. Charact. 142 (2018) 504–514.
[229] S. de Graaf, J. Momand, C. Mitterbauer, S. Lazar, B.J. Kooi, Resolving hydrogen atoms at metal-metal hydride interfaces, Science, Advances 6 (5) (2020) eaay4312.
[230] R.A. Karnesky, P. Chao, D.A. Buchenauer, Hydrogen Isotope Permeation and Trapping in Additively Manufactured Steels, Pressure Vessels and Piping Conference, American Society of Mechanical Engineers, 2017, p. V06AT06A019.
[231] W. Lisowski, A. Van den Berg, D. Leonard, H. Mathieu, Characterization of titanium hydride films covered by nanoscale evaporated Au layers: ToF-SIMS, XPS and AES depth profile analysis, Surface and Interface Analysis: An International Journal devoted to the development and application of techniques for the analysis of surfaces, interfaces and thin films 29 (4) (2000) 292–297.
[232] Y. Duan, W. Wang, J. Liu, S. Peng, L. Shi, IBA investigation on the effect of Ti-Mo interdiffusion on the D concentration in TiDx/Mo films, Nucl. Instrum. Methods Phys. Res., Sect. B 470 (2020) 61–65.
[233] F. Vollnhals, J.-N. Audinot, T. Wirtz, M. Mercier-Bonin, I. Fourquaux, B. Schroeppel, U. Kraushaar, V. Lev-Ram, M.H. Ellisman, S. Eswara, Correlative microscopy combining secondary ion mass spectrometry and electron microscopy: comparison of intensity–hue–saturation and Laplacian pyramid methods for image fusion, Anal. Chem. 89 (20) (2017) 10702–10710.
[234] N. Klingner, R. Heller, G. Hlawacek, S. Facsko, J. von Borany, Time-of-flight secondary ion mass spectrometry in the helium ion microscope, Ultramicroscopy 198 (2019) 10–17.
[235] D. Duca, C. Irimiea, A. Faccinetto, J. Noble, M. Vojkovic, Y. Carpentier, I. K. Ortega, C. Pirim, C. Focsa, On the benefits of using multivariate analysis in mass spectrometric studies of combustion-generated aerosols, Faraday Discuss. 218 (2019) 115–137.
[236] F. Walther, R. Koerver, T. Fuchs, S. Ohno, J. Sann, M. Rohnke, W.G. Zeier, J.r. Janek, Visualization of the interfacial decomposition of composite cathodes in argyrodite-based all-solid-state batteries using time-of-flight secondary-ion mass spectrometry, Chemistry of Materials 31(10) (2019) 3745-3755.
[237] P. Benettoni, H. Stryhanyuk, S. Wagner, F. Kollmer, J.H.M. Osorio, M. Schmidt, T. Reemtsma, H.-H. Richnow, Identification of nanoparticles and their localization in algal biofilm by 3D-imaging secondary ion mass spectrometry, J. Anal. At. Spectrom. 34 (6) (2019) 1098–1108.
[238] A. Castellanos, C.E. Ramirez, V. Michalkova, M. Nouzova, F.G. Noriega, F. Fernández-Lima, Three dimensional secondary ion mass spectrometry imaging (3D-SIMS) of Aedes aegypti ovarian follicles, J. Anal. At. Spectrom. 34 (5) (2019) 874–883.
[239] F. Stevie, Secondary ion mass spectrometry: Applications for depth profiling and surface characterization, Momentum Press2015.
[240] Y. Aboura, D.F. Martelo, R. Morana, R. Akid, K.L. Moore, Characterising hydrogen induced cracking of alloy 625+ using correlative SEM-EDX and NanoSIMS, Corros. Sci. 181 (2021), 109228.
[241] L. Sangely, B. Boyer, E. de Chambost, N. Valle, J.-N. Audinot, T. Ireland, M. Wiedenbeck, J. Aléon, H. Jungnickel, J.-P. Barnes, Secondary ion mass spectrometry, Sector field mass spectrometry for elemental and isotopic analysis2014, pp. 439-499.
[242] S. Fearn, An introduction to time-of-flight secondary ion mass spectrometry (ToF-SIMS) and its application to materials science, Morgan & Claypool Publishers San Rafael, CA, USA2015.
[243] Y. Aboura, K.L. Moore, NanoSIMS analysis of hydrogen and deuterium in metallic alloys: Artefacts and best practice, Appl. Surf. Sci. 557 (2021), 149736.
[244] B. Gault, M.P. Moody, J.M. Cairney, S.P. Ringer, Atom probe microscopy, Springer Science & Business Media2012.
[245] G. Sundell, M. Thuvander, H.-O. Andrén, Hydrogen analysis in APT: methods to control adsorption and dissociation of H2, Ultramicroscopy 132 (2013) 285–289.
[246] J. Takahashi, K. Kawakami, Y. Kobayashi, T. Tarui, The first direct observation of hydrogen trapping sites in TiC precipitation-hardening steel through atom probe tomography, Scr. Mater. 63 (3) (2010) 261–264.
[247] Y.-S. Chen, D. Haley, S.S. Gerstl, A.J. London, F. Sweeney, R.A. Wepf, W. M. Rainforth, P.A. Bagot, M.P. Moody, Direct observation of individual hydrogen atoms at trapping sites in a ferritic steel, Science 355 (6330) (2017) 1196–1199.
[248] I.E. McCarroll, P. Bagot, A. Devaraj, D.E. Perea, J. Cairney, New frontiers in atom probe tomography: A review of research enabled by cryo and/or vacuum transfer systems, Materials Today Advances 7 (2020), 100090.
[249] D. Schreiber, D. Perea, J. Ryan, J. Evans, J. Vienna, A method for site-specific and cryogenic specimen fabrication of liquid/solid interfaces for atom probe tomography, Ultramicroscopy 194 (2018) 89–99.
[250] D.E. Perea, D.K. Schreiber, J.V. Ryan, M.G. Wirth, L. Deng, X. Lu, J. Du, J. D. Vienna, Tomographic mapping of the nanoscale water-filled pore structure in corroded borosilicate glass, npj Mater. Degrad. 4 (1) (2020) 1–7.
[251] P.J. Felfer, A Toolchain for the Analysis of Hydrogen in Materials at the Atomic Scale, Microsc. Microanal. 25 (S2) (2019) 278–279.
[252] M.J. Zachman, N. De Jonge, R. Fischer, K.L. Jungjohann, D.E. Perea, Cryogenic specimens for nanoscale characterization of solid–liquid interfaces, MRS Bull. 44 (12) (2019) 949–955.
[253] C.G. Marxer, M.L. Kraft, P.K. Weber, I.D. Hutcheon, S.G. Boxer, Supported membrane composition analysis by secondary ion mass spectrometry with high lateral resolution, Biophys. J . 88 (4) (2005) 2965–2975.
[254] S.G. Boxer, M.L. Kraft, P.K. Weber, Advances in imaging secondary ion mass spectrometry for biological samples, Annu. Rev. Biophys. 38 (2009) 53–74.
[255] J. Nuñez, R. Renslow, J.B. Cliff III, C.R. Anderton, NanoSIMS for biological applications: current practices and analyses, Biointerphases 13 (3) (2018) 03B301.
[256] G. Williams, H. McMurray, R. Newman, Surface oxide reduction by hydrogen permeation through iron foil detected using a scanning Kelvin probe, Electrochem. Commun. 27 (2013) 144–147.
[257] R. Schaller, J. Scully, Spatial determination of diffusible hydrogen concentrations proximate to pits in a Fe–Cr–Ni–Mo steel using the scanning Kelvin probe, Electrochem. Commun. 63 (2016) 5–9.
[258] C. Larignon, J. Alexis, E. Andrieu, L. Lacroix, G. Odemer, C. Blanc, Investigation of Kelvin probe force microscopy efficiency for the detection of hydrogen ingress by cathodic charging in an aluminium alloy, Scr. Mater. 68 (7) (2013) 479–482.
[259] A. Oudriss, F. Martin, X. Feaugas, Experimental Techniques for Dosage and Detection of Hydrogen, Mechanics-Microstructure-Corrosion Coupling, Elsevier2019, pp. 245-268.
[260] Z. Hua, S. Zhu, B. An, T. Iijima, C. Gu, J. Zheng, The finding of hydrogen trapping at phase boundary in austenitic stainless steel by scanning Kelvin probe force microscopy, Scr. Mater. 162 (2019) 219–222.
[261] L. Oger, M.C. Lafouresse, G. Odemer, L. Peguet, C. Blanc, Hydrogen diffusion and trapping in a low copper 7xxx aluminium alloy investigated by Scanning Kelvin Probe Force Microscopy, Mater. Sci. Eng., A 706 (2017) 126–135.
[262] L. Oger, B. Malard, G. Odemer, L. Peguet, C. Blanc, Influence of dislocations on hydrogen diffusion and trapping in an Al-Zn-Mg aluminium alloy, Mater. Des. 180 (2019), 107901.
[263] M. Duportal, A. Oudriss, X. Feaugas, C. Savall, On the estimation of the diffusion coefficient and distribution of hydrogen in stainless steel, Scr. Mater. 186 (2020) 282–286.
[264] Y. Wang, M. Nastasi, Handbook of modern ion beam materials analysis, Materials Research Society Warrendale, PA2009.
[265] A. Lopez-Suarez, J. Rickards, R. Trejo-Luna, Analysis of hydrogen absorption by Ti and Ti–6Al–4V using the ERDA technique, Int. J. Hydrogen Energy 28 (10) (2003) 1107–1113.
[266] M. Topić, S. Halindintwali, C. Mtshali, S. Nsengiyumva, Z. Khumalo, Hydrogen storage in Ti-based metal hydrides investigated by elastic recoil detection analysis (ERDA), Nucl. Instrum. Methods Phys. Res., Sect. B 450 (2019) 239–243.
[267] C. Jiménez, F. Garcia-Moreno, B. Pfretzschner, M. Klaus, M. Wollgarten, I. Zizak, G. Schumacher, M. Tovar, J. Banhart, Decomposition of TiH2 studied in situ by synchrotron X-ray and neutron diffraction, Acta Mater. 59 (16) (2011) 6318–6330.
[268] K. Herbrig, C. Pohlmann, Ł. Gondek, H. Figiel, N. Kardjilov, A. Hilger, I. Manke, J. Banhart, B. Kieback, L. Röntzsch, Investigations of the structural stability of metal hydride composites by in-situ neutron imaging, J. Power Sources 293 (2015) 109–118.
[269] N. Buitrago, J. Santisteban, A. Tartaglione, J. Marín, L. Barrow, M. Daymond, M. Schulz, M. Grosse, A. Tremsin, E. Lehmann, Determination of very low concentrations of hydrogen in zirconium alloys by neutron imaging, J. Nucl. Mater. 503 (2018) 98–109.
[270] E. Stepanova, N. Pushilina, M. Syrtanov, R. Laptev, E. Kashkarov, Hydrogen effect on Ti-6.5 Al-3.5 Mo-1.5 Zr-0.3 Si parts produced by electron beam melting, Int. J. Hydrogen Energy 44 (55) (2019) 29380–29388.
[271] K. Colas, A.T. Motta, J. Almer, M. Daymond, M. Kerr, A. Banchik, P. Vizcaino, J. Santisteban, In situ study of hydride precipitation kinetics and re-orientation in Zircaloy using synchrotron radiation, Acta Mater. 58 (20) (2010) 6575–6583.
[272] M.V. Alvarez, J. Santisteban, P. Vizcaino, A. Flores, A. Banchik, J. Almer, Hydride reorientation in Zr2. 5Nb studied by synchrotron X-ray diffraction, Acta Mater. 60 (20) (2012) 6892–6906.
[273] J. Kim, J. Kang, C.C. Tasan, Hydride formation in Ti6Al4V: An in situ synchrotron X-ray diffraction study, Scripta Materialia 193 12-16.
[274] M.S. Blackmur, M. Preuss, J.D. Robson, O. Zanellato, R.J. Cernik, F. Ribeiro, J. Andrieux, Strain evolution during hydride precipitation in Zircaloy-4 observed with synchrotron X-ray diffraction, J. Nucl. Mater. 474 (2016) 45–61.
[275] A. Ulvestad, A. Singer, H.-M. Cho, J.N. Clark, R. Harder, J. Maser, Y.S. Meng, O. G. Shpyrko, Single particle nanomechanics in operando batteries via lensless strain mapping, Nano Lett. 14 (9) (2014) 5123–5127.
[276] J. Clark, L. Beitra, G. Xiong, A. Higginbotham, D. Fritz, H. Lemke, D. Zhu, M. Chollet, G. Williams, M. Messerschmidt, Ultrafast three-dimensional imaging

of lattice dynamics in individual gold nanocrystals, Science 341 (6141) (2013) 56–59.
[277] A. Ulvestad, M. Welland, W. Cha, Y. Liu, J. Kim, R. Harder, E. Maxey, J. Clark, M. Highland, H. You, Three-dimensional imaging of dislocation dynamics during the hydriding phase transformation, Nat. Mater. 16 (5) (2017) 565–571.
[278] T. Mazza, P. Piseri, G. Bongiorno, L. Ravagnan, M. Amati, M. Devetta, C. Lenardi, M. Coreno, M. de Simone, P. Milani, Probing the chemical reactivity of free titanium clusters by x-ray absorption spectroscopy, Appl. Phys. A 92 (3) (2008) 463–471.
[279] W. Lanford, Analysis for hydrogen by nuclear reaction and energy recoil detection, Nucl. Instrum. Methods Phys. Res., Sect. B 66 (1–2) (1992) 65–82.
[280] M. Wilde, S. Ohno, S. Ogura, K. Fukutani, H. Matsuzaki, Quantification of hydrogen concentrations in surface and interface layers and bulk materials through depth profiling with nuclear reaction analysis, Journal of visualized experiments: JoVE (109) (2016).
[281] L.-Q. Chen, Phase-field models for microstructure evolution, Annu. Rev. Mater. Res. 32 (1) (2002) 113–140.
[282] T.W. Heo, S. Bhattacharyya, L.-Q. Chen, A phase-field model for elastically anisotropic polycrystalline binary solid solutions, Phil. Mag. 93 (13) (2013) 1468–1489.
[283] T.W. Heo, L.-Q. Chen, Phase-field modeling of displacive phase transformations in elastically anisotropic and inhomogeneous polycrystals, Acta Mater. 76 (2014) 68–81.
[284] O. Takeda, T.H. Okabe, Current status of titanium recycling and related technologies, JOM 71 (6) (2019) 1981–1990.
[285] A. El Kharbachi, E. Dematteis, K. Shinzato, S. Stevenson, L. Bannenberg, M. Heere, C. Zlotea, P.A. Szilágyi, J.-P. Bonnet, W. Grochala, Metal hydrides and related materials. Energy carriers for novel hydrogen and electrochemical storage, ACS Publications, 2020.
[286] M. Kaur, K. Singh, Review on titanium and titanium based alloys as biomaterials for orthopaedic applications, Mater. Sci. Eng., C 102 (2019) 844–862.
[287] J. Bair, M.A. Zaeem, M. Tonks, A review on hydride precipitation in zirconium alloys, J. Nucl. Mater. 466 (2015) 12–20.
[288] A.T. Motta, L. Capolungo, L.-Q. Chen, M.N. Cinbiz, M.R. Daymond, D.A. Koss, E. Lacroix, G. Pastore, P.-C.-A. Simon, M.R. Tonks, Hydrogen in zirconium alloys: A review, J. Nucl. Mater. 518 (2019) 440–460.
[289] X. Ma, S.-Q. Shi, C. Woo, L. Chen, Effect of applied load on nucleation and growth of γ-hydrides in zirconium, Comput. Mater. Sci. 23 (1–4) (2002) 283–290.
[290] X. Ma, S.-Q. Shi, C. Woo, L. Chen, Phase-field simulation of hydride precipitation in bi-crystalline zirconium, Scr. Mater. 47 (4) (2002) 237–241.
[291] X. Ma, S.-Q. Shi, C. Woo, L. Chen, The phase field model for hydrogen diffusion and γ-hydride precipitation in zirconium under non-uniformly applied stress, Mech. Mater. 38 (1–2) (2006) 3–10.
[292] X. Guo, S.-Q. Shi, Q. Zhang, X. Ma, An elastoplastic phase-field model for the evolution of hydride precipitation in zirconium, Part I: Smooth specimen, Journal of Nuclear Materials 378 (1) (2008) 110–119.
[293] X. Guo, S.-Q. Shi, Q. Zhang, X. Ma, An elastoplastic phase-field model for the evolution of hydride precipitation in zirconium, Part II: specimen with flaws, Journal of Nuclear Materials 378 (1) (2008) 120–125.
[294] L. Thuinet, A. De Backer, A. Legris, Phase-field modeling of precipitate evolution dynamics in elastically inhomogeneous low-symmetry systems: Application to hydride precipitation in Zr, Acta Mater. 60 (13–14) (2012) 5311–5321.
[295] L. Thuinet, A. Legris, L. Zhang, A. Ambard, Mesoscale modeling of coherent zirconium hydride precipitation under an applied stress, J. Nucl. Mater. 438 (1–3) (2013) 32–40.
[296] J. Bair, M.A. Zaeem, D. Schwen, Formation path of δ hydrides in zirconium by multiphase field modeling, Acta Mater. 123 (2017) 235–244.
[297] S.-Q. Shi, Z. Xiao, A quantitative phase field model for hydride precipitation in zirconium alloys: Part I. Development of quantitative free energy functional, J. Nucl. Mater. 459 (2015) 323–329.
[298] Z. Xiao, M. Hao, X. Guo, G. Tang, S.-Q. Shi, A quantitative phase field model for hydride precipitation in zirconium alloys: Part II. Modeling of temperature dependent hydride precipitation, J. Nucl. Mater. 459 (2015) 330–338.
[299] G. Han, Y. Zhao, C. Zhou, D.-Y. Lin, X. Zhu, J. Zhang, S. Hu, H. Song, Phase-field modeling of stacking structure formation and transition of δ-hydride precipitates in zirconium, Acta Mater. 165 (2019) 528–546.
[300] C. Qiu, S.M. Opalka, O.M. Løvvik, G.B. Olson, Thermodynamic modeling of the Na–Al–Ti–H system and Ti dissolution in sodium alanates, Calphad 32 (4) (2008) 624–636.
[301] X. Han, Q. Wang, D. Sun, T. Sun, Q. Guo, First-principles study of hydrogen diffusion in alpha Ti, Int. J. Hydrogen Energy 34 (9) (2009) 3983–3987.
[302] J. Chapman, N. Goldman, B.C. Wood, Efficient and universal characterization of atomic structures through a topological graph order parameter, npj Comput. Mater. 8 (1) (2022) 37.
[303] P. Lu, S. Sharifi-Asl, B. Kursten, D.D. Macdonald, The irreversibility of the passive state of carbon steel in the alkaline concrete pore solution under simulated anoxic conditions, J. Electrochem. Soc. 162 (10) (2015) C572.
[304] T.W. Heo, A. Grieder, B. Wang, M. Wood, T. Hsu, S.A. Akhade, L.F. Wan, L.-Q. Chen, N. Adelstein, B.C. Wood, Microstructural impacts on ionic conductivity of oxide solid electrolytes from a combined atomistic-mesoscale approach, npj Comput. Mater. 7 (1) (2021) 214.
[305] P. Modi, K.-F. Aguey-Zinsou, Titanium-iron-manganese (TiFe0.85Mn0.15) alloy for hydrogen storage: Reactivation upon oxidation, Int. J. Hydrogen Energy 44 (31) (2019) 16757–16764.
[306] T.W. Heo, S.A. Khairallah, R. Shi, J. Berry, A. Perron, N.P. Calta, A.A. Martin, N. R. Barton, J. Roehling, T. Roehling, J.-L. Fattebert, A. Anderson, A.L. Nichols, S. Wopschall, W.E. King, J.T. McKeown, M.J. Matthews, A mesoscopic digital twin that bridges length and time scales for control of additively manufactured metal microstructures, Journal of Physics: Materials 4 (3) (2021), 034012.
[307] T.W. Heo, S. Bhattacharyya, L.-Q. Chen, A phase field study of strain energy effects on solute–grain boundary interactions, Acta Mater. 59 (20) (2011) 7800–7815.
[308] T.W. Heo, L.-Q. Chen, B.C. Wood, Phase-field modeling of diffusional phase behaviors of solid surfaces: A case study of phase-separating LiXFePO4 electrode particles, Comput. Mater. Sci. 108 (2015) 323–332.